AIAA JOURNAL
Vol. 62, No. 2, February 2024

Response of a Turbulent Boundary Layer to an Imposed Synthetic Large-Scale Structure

Mitchell Lozier,* Flint O. Thomas,† and Stanislav Gordeyev‡
University of Notre Dame, Notre Dame, Indiana 46556

https://doi.org/10.2514/1.J062916

The dynamic response of a zero-pressure gradient turbulent boundary layer (TBL) to an active flow control actuator was experimentally investigated. The experimental TBL had a sufficiently low momentum thickness Reynolds number, such that there were no energetic organized large-scale structures in the outer region, as evidenced from measurements of the premultiplied wavenumber–frequency spectra. The periodically pulsed plasma actuator, placed inside the outer region of TBL, introduced a synthetic large-scale structure, and the boundary-layer response to this synthetic structure downstream of the actuator at select wall-normal and streamwise locations was investigated. The turbulence amplitude modulating effect of the synthetic large-scale structure, within the inner and log-linear regions of the boundary layer, was isolated and analyzed using a phase-locked analysis. The dynamic interaction of the synthetic large-scale structure and smaller-scale turbulent motions was quantified using a modulation coefficient, and a strong positive correlation within the inner and log regions of the boundary layer was measured. The streamwise development of the synthetic large-scale structure and its modulating effect on the near-wall turbulence across several streamwise locations are described. Profiles of the phase speed at these streamwise locations were extracted and were found to be constant within the log region, further confirming a strong coupling between the near-wall fluctuations in turbulence intensity and the synthetic large-scale motions introduced in the outer region. Overall, the turbulence amplitude modulation effect induced by the synthetic large-scale structure was found to be dynamically similar to the large-scale modulation measured in canonical TBLs at higher Reynolds numbers.

Nomenclature

C_f	=	friction coefficient
f_{LS}	=	large-scale frequency
f_P	=	actuation frequency
f_{SS}	=	small-scale frequency
f_s	=	sampling frequency
H	=	actuator height
H_S	=	boundary-layer shape factor
k	=	wavenumber
L	=	actuator length
l	=	hot-wire length
n	=	single actuation period length realization
Re_θ	=	displacement thickness Reynolds number
Re_τ	=	friction velocity Reynolds number
T_P	=	actuation period
T_s	=	sampling time
t_n	=	time within single actuation period
U	=	mean velocity
U_∞	=	freestream velocity
U_c	=	convective velocity
u	=	streamwise velocity
u_{RMS}	=	root-mean-square of velocity
$u_{\max}$	=	maximum jet velocity
$\tilde{u}$	=	modal component of velocity
u'	=	fluctuating component of velocity
u_τ	=	friction velocity
u_φ	=	phase velocity
v	=	wall-normal velocity
W	=	actuator width
w	=	wake or jet half-width
X	=	global streamwise distance
x	=	streamwise coordinate
x_P	=	pseudospatial streamwise coordinate
y	=	wall-normal coordinate
z	=	spanwise coordinate
δ	=	boundary-layer thickness
Δt	=	time between measurements
$\Delta U_{\max}$	=	maximum wake velocity deficit
$\Delta u'_{\mathrm{RMS}}$	=	residual turbulence
λ_x	=	streamwise wavelength
ν	=	kinematic viscosity
Φ	=	modulation coefficient
Φ_{xx}	=	streamwise power spectral density
φ	=	phase of actuation cycle
$(\cdot)^+$	=	quantity normalized by inner variables
$(\cdot)^*$	=	quantity normalized by outer variables
$\langle\cdot\rangle_n$	=	ensemble average of realizations
$\langle\cdot\rangle_\varphi$	=	phase average

I. Introduction

LARGE-SCALE structures (LSSs), also referred to as large-scale motions (LSMs), are found in the turbulent boundary layer (TBL), and their effect on technologically relevant flow properties such as skin friction drag has been investigated extensively [1–6]. LSS refers in general to organized and energetic spatially coherent motions with a streamwise extent on the order of a few boundary-layer thicknesses ($\lambda_x = 2 - 6\delta$) [5,7] that are found in TBLs with high-enough Reynolds numbers ($Re_\tau > 2000$) [4,5]. The form that these LSSs take at different distances from the wall is shown schematically in Fig. 3 of Ref. [8]. In the outer region of the TBL, the LSS takes the form of groups of spanwise-oriented vortices, with the highest degree of organization and energy contribution typically being observed around the geometric center of the log-linear region of the TBL ($y^+ = 3.9Re_\tau^{0.5}$) [9,10]. Closer to the wall, the coherent structure of the TBL is associated with streamwise vortices located in

Presented as Paper 2021-1455 at the AIAA SciTech 2021 Forum, Virtual Event, January 11–21, 2021; received 17 February 2023; revision received 1 October 2023; accepted for publication 4 October 2023; published online 20 December 2023.

*Graduate Student, Department of Aerospace and Mechanical Engineering; mlozier@nd.edu. Student Member AIAA (Corresponding Author).

†Professor, Department of Aerospace and Mechanical Engineering. Associate Fellow AIAA.

‡Associate Professor, Department of Aerospace and Mechanical Engineering. Associate Fellow AIAA.

the buffer region that have a typical spanwise extent less than boundary-layer thickness [4]. These near-wall streamwise vortical structures are responsible for the large production of turbulence near the wall. Specifically, they transport momentum, leading to higher wall shear stress at the wall and associated skin friction [8], as well as increasing the production of turbulent kinetic energy via enhancing both the sweep and ejection events in the TBL [6,7]. They also have a significant effect on the global boundary-layer dynamics, as noted in many studies [1,4]. Individual coherent vortical structures, often idealized as having a shape that resembles a hairpin, have been observed in TBLs and were found to contribute to both the near-wall and LSSs within the TBL [11]. It has also been shown that the LSSs have a significant interaction with the near-wall structure, and the strength of this interaction grows with Reynolds number [3,12]. It was demonstrated that the LSSs alter turbulence characteristics by imposing mean velocity changes on the near-wall region, referred to as superposition, and by directly modulating the amplitude and organization of the near-wall turbulent motions [3,13].

It is worth noting that in addition to LSSs, which are on the order of several boundary-layer thicknesses, the TBL can also have very long, on the order of $\lambda_x > 6\delta$, flow features consisting of narrow regions of low-streamwise-momentum fluid. These flow features are typically labeled as very large-scale motion (VLSM); the possible relation between LSS and VLSM is currently an active area of research (see a comprehensive review [5] and the references therein, for instance).

In canonical TBLs, thin shear layers were found to separate low-speed and high-speed regions within the TBL, referred to as regions of uniform momentum [9,10]. These thin shear layer structures, combined with the low-momentum flow underneath them, are believed to be part of a coherent structure, referred to as the "attached eddy" [14]. A recent investigation of adverse pressure gradient (APG) TBLs demonstrated that the local flow physics is largely dominated by an embedded shear layer associated with the inflectional instability of the outer mean velocity profile inflection point [15]. Using scaling laws developed for free shear layers and applied to the APG TBL, it was found that the profiles of mean velocity and turbulence quantities exhibited a collapse. The generic applicability of the embedded shear layer scaling was demonstrated by collapsing multiple APG TBL data sets from the AFOSR-IFP-Stanford Conference compiled by Coles and Hirst [16]. Collectively, these results suggest that embedded shear layers are a generic feature of all TBLs, irrespective of whether the mean velocity profile is inflectional. Transient and nonlocalized inflectional instabilities could account for the enhancement of outer large-scale boundary-layer structures that have been documented in previous studies of high-Reynolds-number zero-pressure-gradient TBLs [9,10]. Overall, these shear-layer-like structures likely play an important role in determining LSS dynamics and ultimately in the global properties of all TBLs.

An intriguing aspect of the presence of shear layers in the TBL is that they are amenable to control. The ability to independently control the outer layer LSS in the TBL offers new possibilities for uncovering the underlying dynamics, with particular focus on the outer–inner layer interaction. This aspect has been largely unexplored since most studies and models regarding the relationship between the small-scale structures and LSSs deal with natural or unmanipulated TBLs and apply various conditional-averaging techniques to study their interactions [1,3]. Only a limited number of studies thus far have investigated modifying the coherent structures directly. Some of the first devices used to modify the LSS directly were outer layer devices, sometimes referred to as flat plate manipulators or large-eddy breakup (LEBUs) devices [17]. Studies of these flat plate manipulators in the boundary layer demonstrated that they were effective in modifying or reducing near-wall turbulence-producing events and flow properties such as skin friction drag [18,19] or the optical distortions imposed on a propagating laser beam due to turbulent fluctuations [20]. The most direct effect of these plates was disrupting the LSMs in the outer layer of the TBL, which inhibited high-momentum fluid from being entrained toward the wall, thereby limiting turbulence-producing burst and sweep events [18,19]. Later, in [19] it was shown that while the suppression of LSMs was one mechanism for friction drag reduction, the direct interaction of vortices inside the wake of the LEBU device with near-wall structures provided the primary mechanism. This was supported by the fact that the maximum skin friction reduction occurred at the streamwise location where the wake vortices reached the sublayer. These results suggest that, in general, flat plate manipulators can be used effectively to interrupt the natural interactions that occur between LSSs in the outer layer of the TBL and the small-scale structures near the wall.

Active control devices that introduce periodic LSMs into the TBL are tools that have been used to study the dynamics of the TBL in recent years [21,22]. Large-scale perturbation of the TBL was found to generally have a significant effect on the global TBL dynamics. In one case, large-scale spanwise wall oscillation was able to generate measurable drag reduction with net power savings [21]. In [22–25] a spanwise dynamic roughness element actuated at the wall was used to introduce a periodic traveling wave, or synthetic large-scale structure, into the near-wall and log region of the TBL with a moderately high $Re_\tau \approx 940$ ($Re_\theta \approx 2{,}770$); similar studies were also conducted in a water tunnel at slightly lower $Re_\tau = 410$ ($Re_\theta = 870$) [26]. The frequency of dynamic roughness was selected to introduce organized structures with a streamwise extent of $\lambda_x/\delta = 15$–20, which is comparable to the typical size of VLSM. It was shown that the LSMs induced by the dynamic roughness element resulted in changes to the phase of interactions between triadically coupled modes. Specifically, the synthetic LSMs had the greatest effect on the amplitude of small-scale motions that were triadically coupled with the imposed LSMs, resulting in phase locking with the synthetic mode and hence its reorganization. Importantly, the reorganizing effect was measured, and the mean flow and higher-order statistics retained signatures of the original periodic traveling wave a significant distance downstream of the dynamic roughness location (on the order of 10 TBL thicknesses). Various correlation coefficients were studied [22,24,25] and the existence of the critical layer inside the TBL (where the local speed coincides with the speed of the introduced periodic synthetic mode) was argued to be responsible for the local turbulence modulation. It was also shown that the forcing frequency could be manipulated to generate specific streamwise length scales, which can be selected to excite or organize specific structures related to the near-wall cycle. The results of these dynamic roughness and wall oscillation studies have shown that the TBL is receptive to the introduction of synthetic LSMs. Additionally, these results have shown the synthetic modes can be selectively tuned to have an organizing effect on near-wall small-scale structures that persists a significant distance downstream of the location of the initial perturbation.

In another recent study [27] it was observed that large-scale velocity perturbations *outside of the boundary layer* can also influence near-wall turbulence. In the cited study, a transonic TBL with a high $Re_\tau \sim 7{,}600$ was externally forced by the unsteady pressure field generated from a forced shear layer located well outside of the boundary layer ($y > 4\delta$). The streamwise wavelength of the organized structures induced by the shear layer was $\lambda_x/\delta = 4$–8, which is comparable to the size of naturally occurring LSM and VLSM. Like the dynamic roughness studies discussed above, the near-wall turbulence inside the boundary layer was found to be both amplified and organized by the external forcing due to the excitation of the critical-layer-type velocity mode in the TBL. This result demonstrates that, like the studies of internally forced boundary layers, perturbations to the outer region of the TBL can also cause changes in the amplitude and organization of structures within the near-wall region. However, unlike the studies of internally forced boundary layers, variations in the forced shear layer amplitude, frequency, and position relative to the TBL remained unexplored. In addition, at this high Reynolds number, the TBL has a well-developed natural LSS, and the presence of both the synthetic and the natural LSS could potentially complicate the analysis of the scale interactions inside the TBL.

It is worth noting that, related to the inner–outer scale interaction, there are some studies on turbulent boundary-layer flows interacting with traveling freestream disturbances [28], in which phase organization has also been observed and studied. It was found that the nonlinear effects introduced by the fluctuations were small and the statistics of the velocity field were largely unchanged even for large

fluctuation amplitudes; in other words, the near-wall structure was in-phase with the unsteady freestream flow.

From the previously cited studies, it is clear that the TBL is characterized by the interaction between coherent vortical structures of disparate scales in the outer and inner regions. It remains a topic of some debate, however, regarding the primary driver for such interactions. A so-called "top-down" view holds that the outer LSS dominates and directly influences the near-wall region. In contrast, other studies propose a "bottom-up" approach in which a near-wall autonomous turbulence production mechanism is advocated, which then influences the development of the outer LSS. Understanding the true nature of this inner–outer layer LSS interaction is of primary importance for flow control applications geared toward aerodynamic benefit. To-date, an impediment to full understanding of this inner–outer layer LSS interaction is that most previous studies have been performed in natural, unperturbed TBLs. It stands to reason that if the outer large-scale structure could be made quasi-periodic and thereby provide a well-defined phase reference, then the nature of the inner–outer LSS interaction would become more apparent.

Partially motivated by the studies and results described above, in the current study, an active flow control device is used to introduce large-scale periodic motions into the outer region of a TBL through plasma-jet-based forcing. Plasma actuators have been used both to study fluid dynamics and in flow control applications with great success in recent years [29–32]. In this study, plasma actuation is not employed for aerodynamic benefit but rather as a tool in order to introduce well-defined, organized LSS into the outer portion of the TBL. The synthetically imposed periodic large-scale structure is key to this study since it provides a convenient external phase reference for quantifying the dynamics of the outer–inner layer interaction in the TBL.

The Reynolds number of the experimental TBL in this study was chosen to be $Re_\tau = 690$, which is sufficiently high, so the TBL has the natural near-wall turbulent region, but low enough that there were not naturally occurring, energetic organized LSSs present in the outer region [3]. To study the effect of the large-scale structure on the near-wall region, the actuator is used to introduce a synthetic large-scale structure at user-defined wall-normal positions and with user-defined frequencies. In this way, the bottom-up and/or top-down interactions within the TBL can be fully isolated and studied. In particular, the introduced synthetic LSS was chosen to be representative (in a statistical sense) of the naturally occurring LSS at higher Reynolds numbers. It is worth noting that since the introduced synthetic structure, located in the outer part of the TBL, travels at a higher speed than the near-wall turbulence, the critical-layer mechanism mentioned before will not apply here. Thus, other possible mechanisms of modulating and/or re-organizing the near-wall turbulence can be studied. The present study characterizes the effect of introducing the plasma actuator into the TBL and explores the interaction between the synthetic large-scale structure introduced by the actuator and the near-wall turbulence. It is expected that the spanwise vortices, as part of the synthetic large-scale structure, produced by the actuator will induce large-scale velocity fluctuations throughout the boundary layer, which will lead to a modulation of the small-scale near-wall turbulence amplitude.

II. Experimental Setup

The experiments in this study were performed in one of the low-turbulence, subsonic, in-draft wind tunnels located at the Hessert Laboratory for Aerospace Research at the University of Notre Dame. The wind tunnel has an inlet contraction ratio of 6:1. A series of turbulence-management screens at the front of the inlet give rise to tunnel freestream turbulence levels of less than 0.1% (0.06% for frequencies above 10 Hz). Experiments are performed in a test section of 0.610 m square cross section and 1.82 m length.

The experimental setup is shown schematically in Fig. 1. For this study, a 2-m-long by 0.6-m-wide boundary-layer development plate was installed at the center height of the tunnel test section. The boundary-layer development plate had a sandpaper distributed roughness element attached to the leading edge of the plate, and the leading edge was shaped into a semicircular profile. A constant-

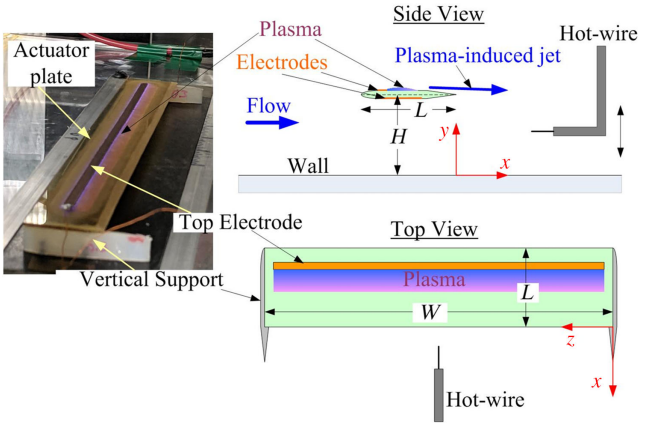

Fig. 1 Photograph and schematic of experimental setup with plasma-based ALSSA device.

temperature anemometer (CTA) with a single boundary-layer hot-wire probe (Dantec 55P15) with diameter 5 μm and length $l = 1.5$ mm (corresponding to $l^+ = 25$) was used to collect streamwise component velocity time-series. As described later, for this hot-wire length, the measured turbulence intensity near the wall, and specifically at its peak value, is expected to be partially attenuated due to spatial filtering [33]. A computer-controlled traversing stage was inserted through the top wall of the tunnel along the midpoint of the tunnel span to allow the hot-wire probe to traverse the test section in the wall-normal direction (y-direction) and make time-resolved velocity measurements within the boundary layer. The minimum step size of the traverse system was 0.00625 mm ($\Delta y^+ = 0.125$), and the wall-normal positioning accuracy of the traverse system relative to the wall was conservatively estimated to be $\varepsilon_y = \pm$ 0.1 mm ($\varepsilon_{y^+} = \pm$ 2) Table A1 in the Appendix.

A plasma-based actuator device, as described in detail below, was attached to the top side of the boundary-layer development plate at a fixed streamwise location of $X = 140$ cm from the leading edge of the boundary-layer development plate. This location was chosen to allow for sufficient streamwise development of the TBL while still leaving sufficient distance downstream of the actuator for the desired measurements. The actuation-based system of coordinates used in this study is shown in Fig. 1. The origin of the streamwise spatial coordinate, x, is located at the plasma actuator's trailing edge. The wall-normal y-axis origin is located at the wall, and the spanwise z-axis origin is located at one spanwise end of the actuator plate, as also shown in Fig. 1. The hot-wire probe was placed downstream of the actuator half-way between the vertical supports to minimize the three-dimensional effects induced by the supports. The streamwise position of the hot-wire probe traverse system was adjustable, so the probe was positioned at four streamwise x-locations to measure the time-resolved TBL response. The locations selected for this study were $x = 51$,102,170, and 272 mm, which correspond to $x/\delta = 1.5, 3, 5$, and 8, respectively, based on the experimentally measured boundary-layer thickness δ at the actuator position.

A set of representative baseline canonical TBL characteristics were measured at the downstream location of $x = 3\delta$ ($X = 1.5$ m from the leading edge of the boundary-layer development plate) using the hot-wire probe. These parameters are summarized in Table 1 for reference. The skin friction velocity u_τ was determined using the Clauser method, and the estimated error in the friction velocity is $\varepsilon_{u_\tau} = \pm$ 9% Table A1 in the Appendix. In all the experiments described in this study, the nominal wind tunnel freestream velocity was 7 m/s and was measured to be within 1% of the expected freestream velocity before each test.

As shown in Fig. 1, a plasma-based active large-scale structure actuator (ALSSA) device was used in this study to introduce periodic plasma-induced forcing in the outer layer of the boundary layer. The plasma actuator was supported above the boundary-layer development plate by vertical NACA0010 airfoils on both sides, which were 4 mm thick and were made at heights H between $H = 10$ and 21 mm

Table 1 Canonical turbulent boundary-layer parameters at $x = 3\delta$

Parameter	Value
δ	33.2 mm
θ	3.9 mm
U_∞	6.95 m/s
u_τ	0.304 m/s
C_f	0.0039
H_s	1.37
Re_θ	1,770
Re	690

(0.3δ and 0.6δ). In this manner, LSMs generated by the actuator, referred to as the synthetic LSS, could be introduced into the TBL at different distances away from the wall. The plasma actuator was $W =$ 25 cm (8δ) wide in the spanwise direction and $L = 32$ mm ($< 1\delta$) long in the streamwise direction. Due to the finite spanwise width of the actuator plate and the presence of the airfoil supports underneath, three-dimensional motions are expected at either end of the plate. The reasoning and significance for choosing these actuator dimensions will be discussed in detail in Sec. IV. The actuator plate was made of a 2-mm-thick sheet of Ultem dielectric polymer, as shown in Fig. 2. An upper surface electrode of 0.05-mm-thick copper foil tape was located 15 mm from the plate leading edge and was 4 mm in length and 22 cm in width. On the lower surface, a second copper foil electrode was located 15 mm from the leading edge in line with the top electrode and was 12 mm in length and 22 cm in width. The positioning of the electrodes with respect to the leading edge of the dielectric plate and the width of the electrodes were carefully selected to prevent arcing between the top and bottom electrodes around the edges of the dielectric plate.

The bottom electrode extends farther downstream than the top electrode to create a region of high potential, which forms the streamwise-oriented plasma jet, as shown in Fig. 2. The corners of the electrodes were rounded, and they were aligned to reduce extraneous regions of plasma and regions of highly concentrated plasma. The leading edge of the actuator plate was rounded, and the last 10 mm of the trailing edge was linearly tapered to a half-angle of 10° to eliminate the separation region downstream of the trailing edge of the actuator plate.

The alternating current dielectric barrier discharge (AC-DBD) plasma formed on the actuator was produced using a high-voltage AC source [34], which consisted of a single-frequency function generator, a modulator, a power amplifier, and a transformer, as schematically shown in Fig. 2. The electrodes on the top and bottom of the actuator were connected to the high-voltage AC source, which provided a 40 kV peak-to-peak sinusoidal waveform excitation to the electrodes at a frequency of 4 kHz. The carrier frequency of 4 kHz was chosen because it creates a quasi-steady plasma jet, irrespective of the modulation applied later to induce periodic forcing [34]. The peak-to-peak voltage was maintained within ±5% of the expected excitation voltage during the experiments. It has been observed that high relative humidity can decrease the body force produced by the actuator [35]. This is noteworthy when discussing the experimental results presented later because the relative humidity in the laboratory,

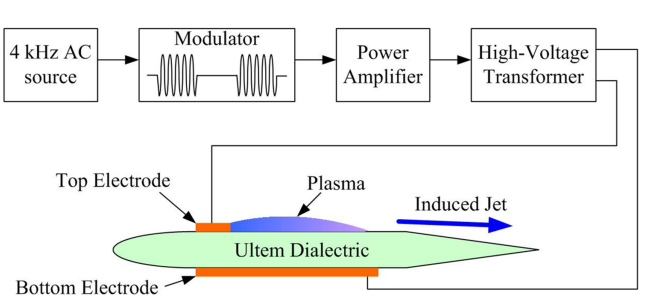

Fig. 2 Schematic of alternating current dielectric barrier discharge (AC-DBD) plasma formation.

which feeds the in-draft wind tunnel, fluctuates between seasons. As shown in Fig. 2, the plasma jet was formed on the top surface of the actuator plate above the exposed portion of the lower surface electrode. Measurements of the plasma jet velocity in still air are presented in Fig. A2 in the Appendix for reference. As mentioned earlier, at the 4 kHz carrier frequency, the plasma actuator operates in a quasi-steady mode, essentially creating a spanwise-uniform steady wall jet in the streamwise direction [34]. To introduce periodic forcing, the sinusoidal waveform was modulated by a square wave using a modulator with a 50% duty cycle oscillating at the prescribed forcing frequency. This modulation, or periodic switching on and off, of the plasma jet will be referred to later as the actuation cycle.

A pitot probe was also inserted into the test section upstream of the plasma actuator through the side wall of the tunnel to determine the freestream velocity of the tunnel for calibration of the hot-wire probe. Hot-wire voltages, pitot probe pressure transducer voltages, and the output of the function generator to the ALSSA device were digitally recorded simultaneously in every experiment. The data were sampled at $f_s = 30$ kHz, which corresponds to $\Delta t^+ = (1/f_s)u_\tau^2/\nu = 0.2$ for a total sampling time T_S of at least 90 s, or about 15,000 δ/U_∞ in each test. With this sampling frequency and sampling time, there should be no additional loss of turbulence information, compounding the spatial averaging effect of the hot-wire length, as described in [33].

III. Data Reduction

The hot wire was calibrated before and after each experiment using standard methods [36], and the anemometer voltages were converted into velocities using a linear interpolation between the two calibrations to account for any drift in laboratory temperature over the course of the experiment. The maximum ambient temperature drift over the course of any experiment was recorded to be 0.2°C, and the maximum ambient pressure drift over any one experiment was 2 mbar. The velocity time series were digitally band-stop filtered between 3.8 and 4.2 kHz to eliminate electronic noise associated with the high-voltage AC source supplying the actuator. After the hot-wire voltages were converted and filtered, the time mean U, the root mean square (RMS) of the velocity u_{RMS}, and skewness of the velocity were calculated at every wall-normal location (y-location) using standard methods. The resulting error in the instantaneous streamwise velocity was conservatively estimated to be $\varepsilon_u < \pm 0.05u_\tau$ ($\varepsilon_u < \pm 0.002U_\infty$) Table A1 in the Appendix. Since the actuator introduced periodic forcing into the flow, it is convenient and necessary to phase-lock the results to the periodic forcing frequency to separate the synthetic LSMs from the small-scale turbulent response [27].

To implement phase-locking, a triple phase-locked Reynolds decomposition of the velocity was considered, as shown in Eq. (1), where u is the instantaneous velocity, U is the time mean component of velocity, $\tilde{u}$ is a phase-dependent or modal velocity component, u' is a residual fluctuating turbulent component, and φ is the phase, defined by the relationship in Eq. (2), where n is the number of realizations.

$$u(y,t) = U(y) + \tilde{u}(y,\varphi) + u'(y,\varphi,n) \tag{1}$$

$$\varphi = \left(\frac{t_n}{T_p} - n\right)2\pi \tag{2}$$

The n realizations are single-actuation-period ($T_p = 1/f_p$) length samples ($f_S/f_P = 375$ time steps per realization) extracted from the overall time series. Each realization is phase-locked with the plasma forcing and begins when the plasma actuator is turned on in the actuation cycle. In Eq. (2), t_n is a time in the nth realization, which is related to a phase angle φ by the period of the actuation cycle. The signal produced by the function generator, which drives the actuation cycle, was recorded and used to ensure the velocity data was phase-locked with the plasma actuation cycle. These n realizations are then ensemble averaged to find the modal component of velocity as a function of the phase angle. The fluctuating component of the velocity u' that remains after removing the modal component of velocity from each realization was used to calculate an ensemble-averaged root-mean-square of the fluctuating velocity shown in Eq. (3).

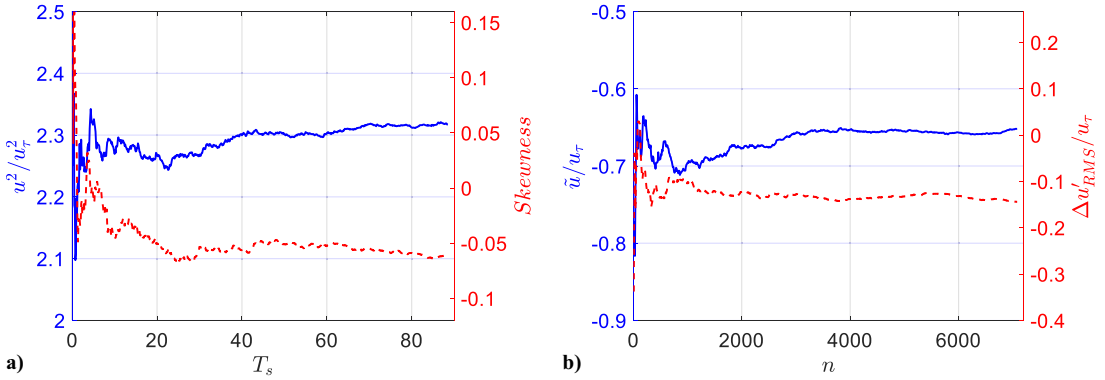

Fig. 3 Convergence of a) turbulence intensity and skewness based on sampling time, and b) modal velocity and residual turbulence based on number of realizations, n. Measured with active plasma forcing at $y^+ = 100$ and $x = 5\delta$. Solid lines correspond to the left axis. Dashed lines correspond to the right axis. $H^+ = 200$, $f_P = 80$ Hz.

$$\Delta u'_{\mathrm{RMS}} = (\langle u'(y,\varphi,n)^2\rangle_n)^{1/2} \tag{3}$$

Here, the angle brackets denote ensemble averaging over all realizations. Later, we will refer to this quantity as the residual turbulence, which represents the small-scale response of the TBL phase-locked with the synthetic large-scale actuation. The phase-averaged mean can be removed from the residual turbulence level to define a local change in residual turbulence. In the present experiments, the sampling time results in $n = 7200$ realizations and was chosen to achieve convergence of the residual turbulence, as demonstrated in Fig. 3b. The skewness, which is the highest-order statistical quantity analyzed in this experiment, also reaches convergence within the prescribed sampling time, as shown in Fig. 3a.

A so-called Φ-coefficient, which was introduced in [9], is used to quantify the modulating effect of the LSMs on phase-locked small-scale motions and is shown in Eq. (4). This modulation coefficient correlates changes in the modal velocity, which represents the synthetic LSMs, to those in the residual turbulence, which represents the phase-locked small-scale response of the TBL. Higher modulation coefficient values indicate that the induced LSMs and phase-locked small-scale responses are in phase. This new modulation coefficient is similar to the modulation coefficients used in other studies [2,24], with the small-scale response being redefined here in a phase-locked scheme. A direct experimental comparison of these coefficients can be found in Fig. 15.

$$\Phi(y) = \frac{\langle \tilde{u}(y,\varphi)\Delta u'_{\mathrm{rms}}(y,\varphi)\rangle_\varphi}{\sqrt{\langle \tilde{u}(y,\varphi)^2\rangle_\varphi}\sqrt{\langle \Delta u'_{\mathrm{rms}}(y,\varphi)^2\rangle_\varphi}} \tag{4}$$

IV. Baseline Measurements

First, the canonical boundary layer, that is, without the ALSSA device, was measured with the hot wire at each measurement location to establish a baseline before adding the passive effect of the actuator plate alone or the active effect of applying plasma forcing. The canonical mean velocity profile and turbulence intensity profiles at the streamwise measurement location of $x = 3\delta$ can be seen in Fig. 4a. There is a well-defined log-linear region in the mean velocity profile from $y^+ = 50$–200, highlighted by the dashed line in Fig. 4a. The measured mean velocity profile also matches the Direct Numerical Simulation (DNS) result [37] with an equivalent Reynolds number well over the entire measurement range. The turbulence intensity profile, u^2_{rms}, is approximately 20% lower than the DNS profile [37] over the entire boundary layer due to the spatial averaging effect of the finite hot-wire length ($l^+ = 25$) [33]. The peak in the turbulence intensity is measured to be around $y^+ = 16$, similar to the DNS result. When the spatial averaging effect is accounted for [33], the compensated peak turbulence intensity, shown as a black "x" in Fig. 4a, matches the DNS result very well, further confirming that the attenuation is due to the finite hot-wire length alone. Later in this paper, we will present only uncompensated turbulence intensity results.

The premultiplied streamwise wavenumber–frequency energy spectra for a single measurement location of $x = 3\delta$ is presented in Fig. 4b. The near-wall or inner energy peak aligns well with the expected location of $y^+ = 16$, $\lambda_x^+ = 1000$ as marked by the white "+" symbol [1]. The theoretical location of the natural LSS, which would be present at higher Reynolds numbers, is at the geometric center of the log region for sufficiently large Reynolds numbers [3], and it is indicated by the circle in Fig. 4b. At the moderately high

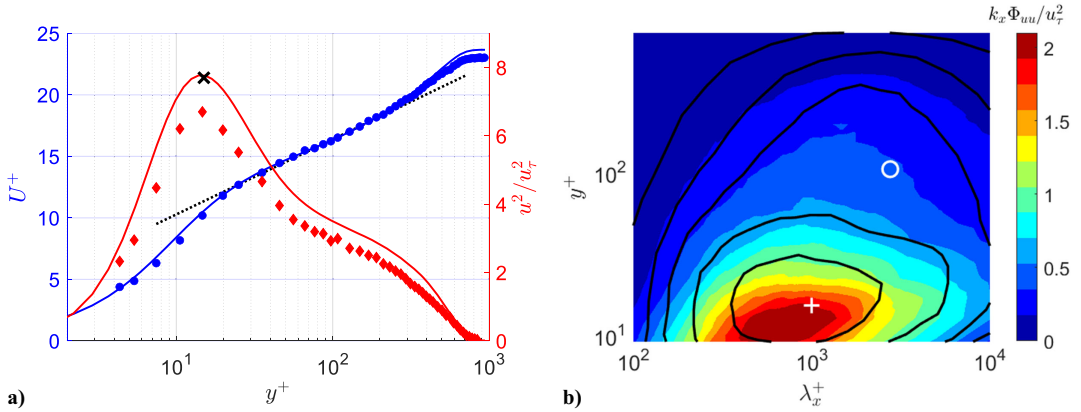

Fig. 4 a) Mean velocity and turbulence intensity profiles measured for canonical boundary layer as filled symbols. DNS results for $Re_\tau = 690$ [37] as solid lines. "X" symbol indicates the compensated peak turbulence intensity. b) Premultiplied streamwise energy spectra measured for the canonical boundary layer at $x = 3\delta$. Symbol "+" marks inner peak ($y^+ = 16$, $\lambda_x^+ = 1000$). Open circle marks theoretical location of outer peak ($y^+ = 3.9Re_\tau^{1/2}$, $\lambda_x^+ \approx 2700$) for $Re_\tau = 690$. Solid contour lines overlaid for $Re_\tau = 1100$ from [3].

Reynolds number of $Re_\tau = 690$ in this experiment, there is no natural coherent large-scale structure present. There are LSMs in the experimental boundary layer, but they do not form an organized and energetic structure like those seen in higher-Reynolds-number TBLs. The streamwise wavelength of the naturally occurring LSS has been reported in the range of $2-6\delta$ in studies of canonical TBLs [1,3], and the streamwise wavelength of $\lambda_x = 4\delta$ ($\lambda_x^+ = 2700$) specifically is identified by the open circle in Fig. 4b. In addition to the quantitative agreement of the premultiplied spectra to expected values, there is also qualitative agreement with other experiments at similar Reynolds numbers [3], as shown by the overlaid contours in Fig. 4b.

V. Actuator Optimization

There were multiple characteristics of the actuator design and operation that had to be tested and optimized before the final configuration of the actuator was chosen, as described in Sec. II. The first of these characteristics was the spanwise width and streamwise length of the physical actuator plate. In preliminary tests, it was found that the wake produced by the plate was a dominant feature of the flow downstream of the actuator (see Fig. A1 in the Appendix). To increase the strength of the plasma forcing relative to the plate's wake and the natural TBL structures, the streamwise length of the plate was reduced to its minimum length for safe operation with the plasma. There should be approximately 5 mm of dielectric per 10 kV excitation voltage separating the electrodes as measured from the electrode's edge around the edges of the dielectric plate to prevent arcing at the voltage used in this experiment [34]. With this constraint, the final streamwise length of the actuator was set to $L = 32$ mm. As discussed above, the goal of this actuator is to introduce spanwise-uniform, two-dimensional motions into the boundary layer. The dielectric material used in the actuator plate does not have the stiffness required to easily span the entire tunnel width without warping or vibrating, so airfoil contoured supports were used to anchor the finite-width actuator plate to the wall. The finite width of the actuator plate and airfoil supports below the actuator plate introduced three-dimensional motions around the ends of the plate. The spanwise extent of the natural LSS in the TBL is on the order of the boundary-layer thickness [4]. The actuator is able to introduce two-dimensional motions that are larger in spanwise coherence than the natural LSS but, at the same time, are locally dynamically consistent with the natural LSS. To investigate the three-dimensional end effects of the plate, the actuator was placed on a traversing stage that could be moved in the spanwise direction (z-direction), while the fixed hot wire measured the spanwise variation in flow downstream of the actuator. Figure 5 shows the reconstructed mean velocity field of the wake behind one of the airfoil supports ($z/\delta = 0$) attached to the end of the actuator plate with no active plasma forcing. Spanwise profiles were taken at a wall-normal distance of $y^+ = 100$ and extend from the airfoil support toward the center of the plate ($-z$) and at least one boundary-layer thickness past the end of the plate ($+z$) at each measurement location. The profiles were interpolated to create a reconstruction of the entire downstream field.

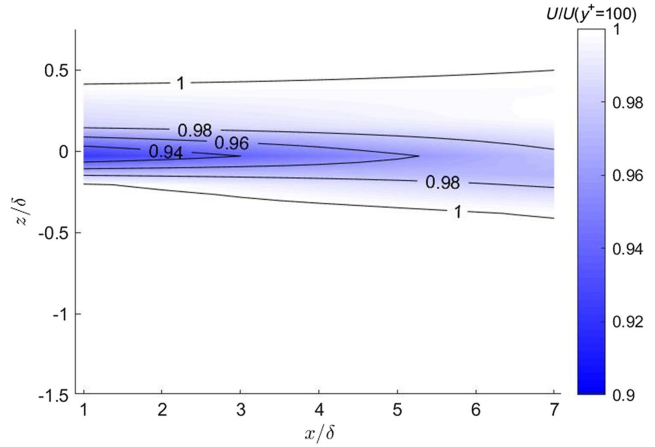

Fig. 5 Spanwise-streamwise reconstruction with isocontours of mean velocity behind airfoil support (located at $z/\delta = 0$), normalized by local mean velocity. Measured at $y^+ = 100$. $H^+ = 200$.

In Fig. 5, the normalized mean velocity field shows that the mean velocity deficit created by the airfoil vertical support is spreading in the spanwise direction downstream of the actuator. Velocity deficits were measured more than one-half of a boundary-layer thickness away from the airfoil support at the farthest downstream point of $x = 8\delta$. The RMS of velocity and the skewness have similar behavior. The same behavior is also observed under active plasma forcing. Assuming that the actuator plate is symmetrical about its center and knowing that, conservatively, at least one boundary-layer thickness from either side of the plate will have induced three-dimensional motions, the final spanwise width of the plate was chosen to be $W = 8\delta$. This actuator width will result in at least a 6δ wide region of approximately two-dimensional, spanwise uniform motions centered around the midpoint of the actuator plate, even at the farthest downstream location.

Along with the actuator plate dimensions, the wall-normal location of the actuator is another important parameter in the experiment. Parametric studies of the effect of the wall-normal actuator location H were conducted and discussed in a previous study [38] to investigate which wall-normal locations result in the strongest modulating effect in the near-wall region. A range of wall-normal positions between $H = 0.3\delta$ and 0.6δ ($H^+ = 200$ and 400) were selected for comparison. The wall-normal position of $H = 0.6\delta$ was chosen for comparison based on the results of flat plate manipulator studies [20], which showed that this location was an optimal wall-normal plate location to reduce large-scale velocity fluctuations downstream of the plate. The second wall-normal position of $H = 0.3\delta$ is near the upper limit of the log-linear region, as measured from the canonical TBL mean velocity profile (see Fig. 4), which is closer to the location of natural LSSs. It is also far enough from the wall to limit unintended secondary effects like significantly accelerating the flow between the plate and the wall. As shown in the study referenced above, there was a 20% reduction in turbulence intensity near the wall, which was attributed to large-scale modulation of the residual turbulence when the plate was at the closest wall-normal position compared to the farthest. There was also a negative shift in the skewness, which is attributed to a change in the dynamics of the nonlinear interactions near the wall. The phase-locking or reorganizing effect below the actuator, as measured by the modulation function Φ, did not change significantly between the different wall-normal positions. Overall, the actuator showed the capability to modulate and organize near-wall turbulence at all locations, but when it was closer to the wall the interactions between the LSS and near-wall structures were stronger. For this reason, the current study is focused only on the wall-normal location $H = 0.3\delta$ ($H^+ = 200$).

Another key parameter of the actuator design, which was expected to have a significant effect on phase locking, was the plasma forcing frequency. The objective of the plasma forcing is to introduce a synthetic large-scale structure at a prescribed frequency and modify the near-wall structures to study the outer–inner interaction mechanism. The canonical boundary-layer flow has two key characteristic frequencies. One is associated with the typical burst-sweep frequency of the small-scale turbulence near the wall. In [39], this small-scale frequency, f_{SS}, was determined to be approximately $f_{SS}^+ = f_{ss}\nu/u_\tau^2 = 0.011$, which would correspond to a frequency of $f_{SS} = 81$ Hz in the current experiment. The other frequency, f_{LS}, is associated with the size of naturally occurring LSSs. The streamwise wavelength of LSSs in the canonical boundary layer was estimated to be around $\lambda_x = 4\delta$ based on measurements in higher-Reynolds-number TBLs [3], making the theoretical large-scale frequency $f_{LS} = U_\infty/\lambda_x = 52$ Hz for the experimental Reynolds number. This results in an outer-scaled, large-scale frequency of $f_{LS}^* = f_{Ls}\delta/U_\infty = 0.25$. It should be noted that, for the moderately low experimental Reynolds number here, these characteristic frequencies are relatively similar. But there is no natural outer large-scale structure present in the experimental TBL, so the characteristic large-scale frequency calculated above is only theoretical. This is shown explicitly through measurements of the premultiplied streamwise velocity spectra presented in Fig. 4b, where

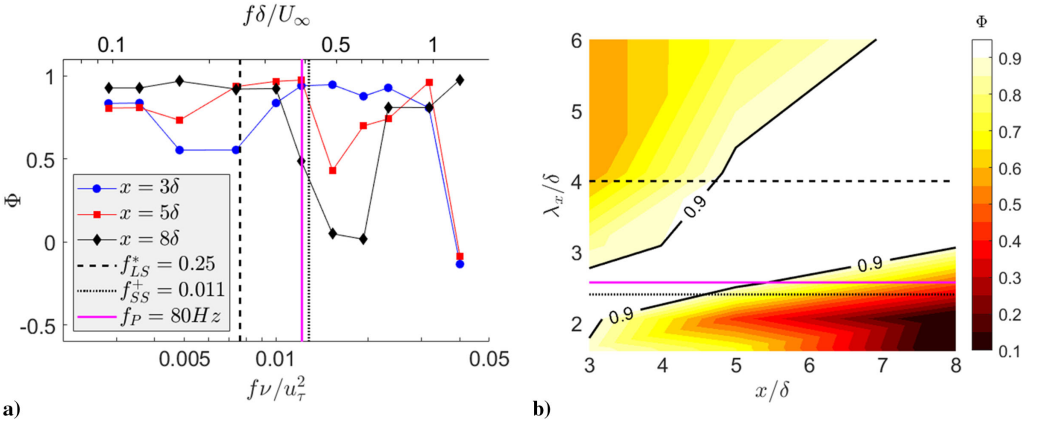

Fig. 6 a) Frequency dependence of Φ coefficient across streamwise locations. Dashed black lines mark $f^*_{LS} = 0.25$. Dotted black lines mark $f^+_{SS} = 0.011$. Solid magenta lines mark $f_P = 80H$. b) Φ coefficient variation with streamwise length scale and streamwise location. Measurements made at $y^+ = 20$. $H^+ = 200$.

no outer peak is seen around the theoretical characteristic large-scale frequency (or corresponding wavelength).

To investigate which frequencies will result in the strongest modulation effect near the wall, the hot-wire probe was placed in the near-wall region at $y^+ = 20$, and the frequency of the plasma forcing was varied from 20 to 200 Hz. For each forcing frequency, the modal velocity and residual turbulence were extracted, and the modulation coefficient Φ [Eq. (4)] was computed. Figure 6a presents the values of the modulation coefficient Φ, measured near the wall, for different forcing frequencies at downstream locations between $x = 3, 5$ and 8δ. There is a band of frequencies around $f^+ = 0.007$–0.011 ($f^* = 0.25$–0.41 or $f = 52$–81 Hz), where the modulation coefficient reaches a peak value ($\Phi > 0.9$) at all streamwise locations. This indicates that the correlation between synthetic LSMs, introduced by the plasma actuator, and the small-scale response near the wall is the strongest for forcing frequencies within this range, regardless of streamwise location. Closer to the actuator plate ($x = 3 - 5\delta$), the frequency of the peak in the modulation coefficient matches the expected near-wall frequency, which is around $f^+ = f\nu/u_\tau^2 = 0.011$ [39] marked by the vertical dotted line in Fig. 6a. Conversely, farther downstream from the plate ($x = 5 - 8\delta$), the frequency of the peak in the modulation coefficient matches the theoretical outer layer frequency of $f^* = f\delta/U_\infty = 0.25$ marked by the vertical dashed line in Fig. 6a. This presents an interesting observation that, immediately downstream of the actuator plate, the near-wall region is most receptive to perturbations with a frequency closely related to the characteristic frequency of the near-wall structures. However, farther downstream, the near-wall region is receptive to larger-scale perturbations on the order of the theoretical characteristic LSS. Based on these results, the forcing frequency was chosen to be $f_P = 80$ Hz ($f^+_P = 0.011$, $f^*_P = 0.39$) for the current experiment. Using Taylor's hypothesis, this forcing frequency corresponds to a synthetic structure of $\lambda_x = 2.5\delta$. Another way to analyze the Φ modulation coefficient is to plot it as a function of the streamwise size of the synthetic structure, computed using Taylor's hypothesis, and streamwise location. These results are presented in Fig. 6b as a contour plot. The scales near the wall, corresponding to high values of $\Phi > 0.9$, monotonically increase downstream of the actuator, approaching values of $\lambda/\delta > 4$ at the farthest downstream location of $x/\delta = 8$. This suggests that the flow structures near the wall gradually adjust to the presence of a synthetic structure, on the order of the theoretical characteristic large-scale.

VI. Results

With the key parameters of the actuator optimized for the purposes of this study, further analysis of the effect of the actuator on the TBL was performed. First, we will discuss the effect of adding the actuator plate without any active plasma forcing. Since the presence of the plate alone will modify the boundary layer, similar to the LEBU devices discussed in the Introduction, the changes in the baseline flow were quantified before evaluating the effect of adding plasma forcing. The plate-only mean velocity, turbulence intensity, and the skewness profiles for two streamwise measurement locations can be seen in Fig. 7 as open symbols. For comparison, the same quantities for the canonical boundary layer are also shown in Fig. 7 as lines. At the actuator plate's wall-normal position, marked by the dashed line, there is a local decrease in mean velocity, shown in inner unit scaling in Fig. 7a and in outer unit scaling in Fig. 7b, and a local increase in turbulence intensity, shown in Fig. 7c. These effects are characteristic of the plate's wake and have been similarly documented for LEBU devices in the past [18]. Figure 7d presents the skewness plots for the canonical, plate-only, and plasma-on cases. The DNS results for a canonical TBL for a similar $Re_\tau = 690$ [37] are shown as a thick black line for comparison; the agreement with the canonical TBL skewness from the current study is excellent. The skewness profiles around the actuator location, shown in Fig. 7d, approach zero downstream of the plate; this is an expected behavior at the center of the plate's symmetric wake. Moving downstream, the mean velocity deficit and increase in turbulence intensity around the actuator plate location tend to recover toward the canonical profile. Below the actuator plate, there is a consistent decrease in turbulence intensity measured at $x = 5\delta$ as compared to $x = 1.5\delta$. The profile of skewness appears to be relatively constant between the two measurement locations.

The development of the plate's wake was isolated by subtracting the canonical statistics from the plate-only statistics at each streamwise location. These results are shown in Fig. A1 in the Appendix for reference and demonstrate that the plate's wake follows a relatively canonical planar wake development even within the TBL.

The momentum thicknesses of the canonical and modified boundary layers were calculated at each streamwise measurement location and are presented in Fig. 8. The momentum thickness of the canonical TBL grows with streamwise distance proportional to $Re_X^{0.2}$. The momentum thickness for the plate-only case is consistently higher than the canonical case because of the momentum deficit induced by the actuator plate, and it is growing at a similar rate. This behavior is consistent with measurements of the effect of LEBU devices [18].

In Fig. 9, the turbulence intensity, normalized by the local mean velocity, has been plotted against the local mean velocity normalized by the freestream velocity, similar to [40]. It is expected that in the canonical TBL there will be a linear relationship between these quantities in the outer region, as demonstrated by the dotted lines in Fig. 9. In the plate-only case, there is a deviation from the linear scaling in the outer region due to the presence of the actuator plate. This effect can be seen at both streamwise locations, immediately downstream of the actuator and farther downstream as well.

The premultiplied spectra for the plate-only case are presented in Figs. 10c and 10d. The spectra appear very similar to the premultiplied spectra for the canonical boundary layer, presented in Figs. 10a and 10b, in the region below the actuator plate. Around the actuator location, indicated by the dashed line, there is weak additional energy

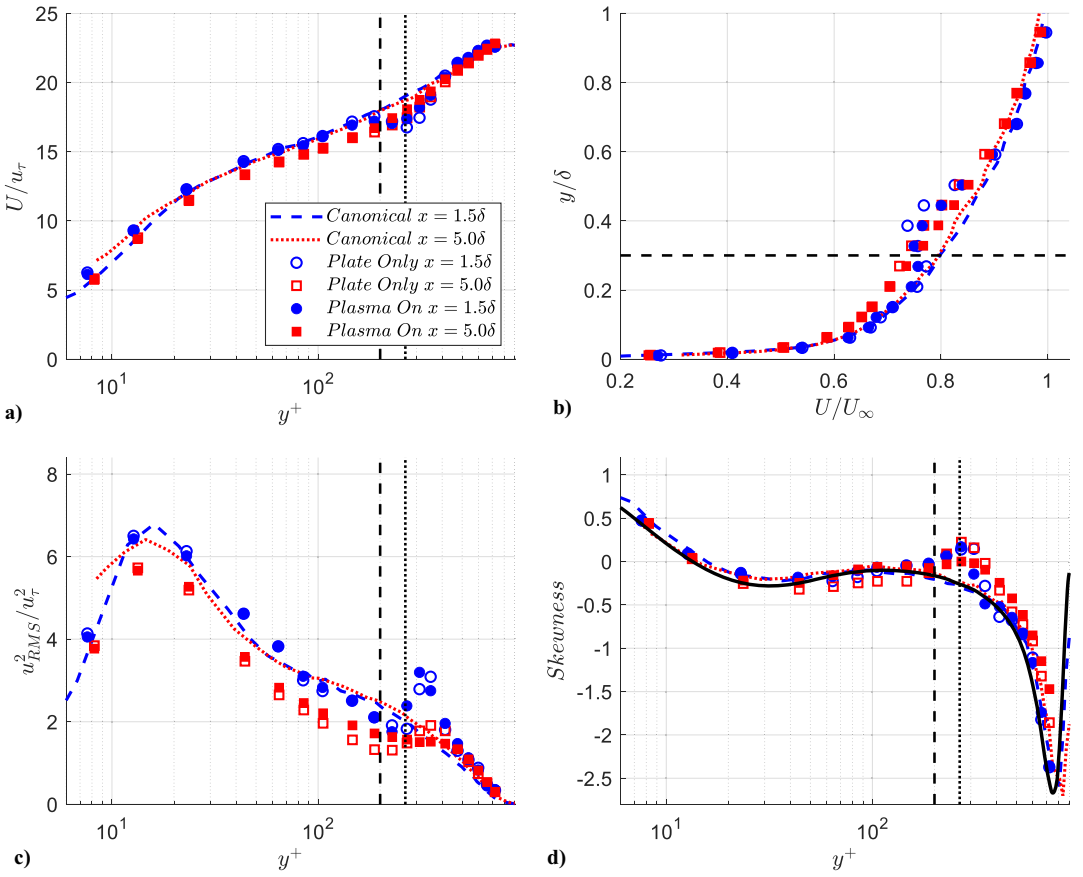

Fig. 7 Profiles of a) inner scaled mean velocity, b) outer scaled mean velocity, c) turbulence intensity, and d) skewness at $x = 1.5\delta$ (blue) and $x = 5\delta$ (red). Canonical (solid line), plate-only (open symbols), and plasma on (filled symbols). Dashed line marks the actuator height, $H^+ = 200$ ($H = 0.3\delta$). Dotted line marks the plasma jet location, $H_P^+ = 265$. $f_P = 80$ Hz. A thick black line in (d) presents DNS results for canonical TBL for $Re_\tau = 690$ [37].

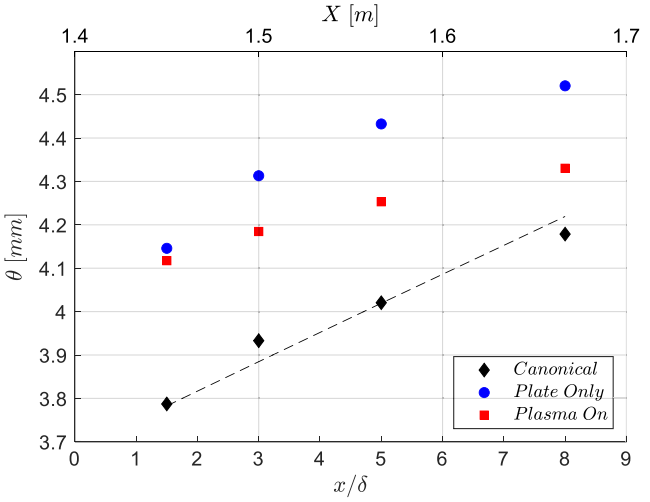

Fig. 8 Streamwise development of momentum thickness θ in canonical and modified turbulent boundary layer. Dashed line represents $\theta/X = 0.037/Re_X^{0.2}$. $H^+ = 200$, $f_P = 80$ Hz.

added by the actuator plate at smaller streamwise wavelengths ($200 < \lambda_x^+ < 500$), primarily above the actuator plate. The full effect of the actuator plate on the baseline flow at different streamwise locations can be more easily seen by looking at the difference in premultiplied spectra between the canonical and plate-only cases, presented in Figs. 11a and 11b. By examining the discrepancy between the plate-only and canonical cases in Fig. 11a at the streamwise location of $x = 1.5\delta$, there is a decrease in the energy of large wavelength motions ($\lambda_x^+ > 500$) and an increase in the energy of smaller wavelength motions ($\lambda_x^+ < 500$). This behavior is consistent with the plate inhibiting LSMs and the generation of smaller-scale motions in the plate's wake, as described in other studies of flat plate manipulators [18,20]. This large-scale suppression persists downstream but starts to weaken and spread in the wall-normal direction farther downstream of the actuator at $x = 5\delta$, as shown in Fig. 11b. This is consistent with the growth of the wake generated by the plate. There is also an immediate suppression of energy around the inner peak location at the closest streamwise location $x = 1.5\delta$ (see Fig. 11a), which recovers farther downstream as the boundary layer adjusts to the presence of the plate.

Once the modified baseline (plate only) was established, the effect of the plasma forcing on the boundary layer was studied. Measurements quantifying the plasma jet in still air are shown in Fig. A2 in the Appendix for reference. The location of the plasma jet ($H_P^+ = 265$) is slightly above the actuator plate ($H^+ = 200$) and indicated by the vertical dotted lines in Fig. 7. The mean velocity, turbulence intensity, and skewness profiles for the plasma on case are presented in Fig. 7 as filled symbols. The addition of the plasma jet partially mitigates the wake-related changes due to the plate. It can be observed in Figs. 7a–7c that the addition of the plasma jet almost recovers the canonical TBL statistics for $y^+ < 200$. At the actuator location, there are small changes to the amplitude of the velocity deficit, the peak in turbulence intensity, and the amplitude of the skewness. These peaks have also been shifted slightly toward the wall due to the presence of the plasma jet on the top side of the actuator plate. These results are expected, as the lack of significant change in statistical quantities has been observed with other actuators where the induced perturbations affect boundary-layer dynamics with little relative change in statistical quantities [23].

The momentum thickness under active plasma forcing was also measured and compared to the canonical and plate-only cases in Fig. 8. With active plasma forcing, the momentum thickness decreased relative to the plate-only case, and the difference between the two cases increased with downstream distance, reaching a constant difference at the farthest downstream location. The decrease in momentum

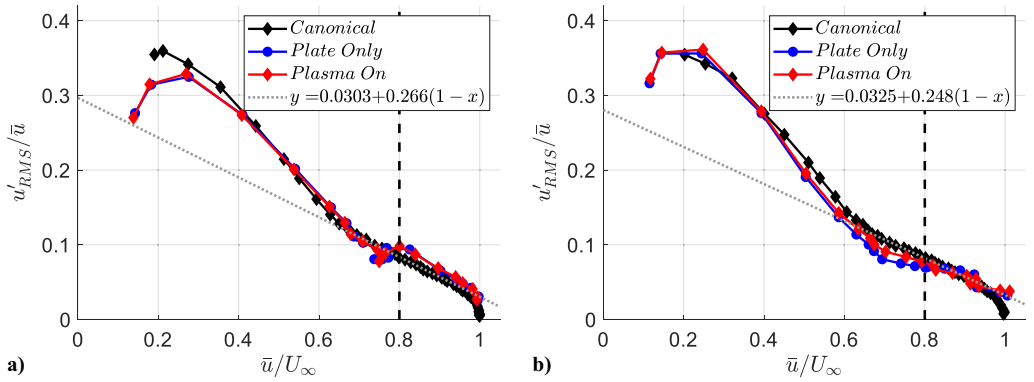

Fig. 9 Normalized turbulence intensity plotted versus normalized mean velocity measured at a) $x = 1.5\delta$ and b) $x = 8\delta$. Actuator location marked by vertical dashed line. Least-squares fit of linear region shown as dotted gray line. $H^+ = 200$, $f_P = 80$ Hz.

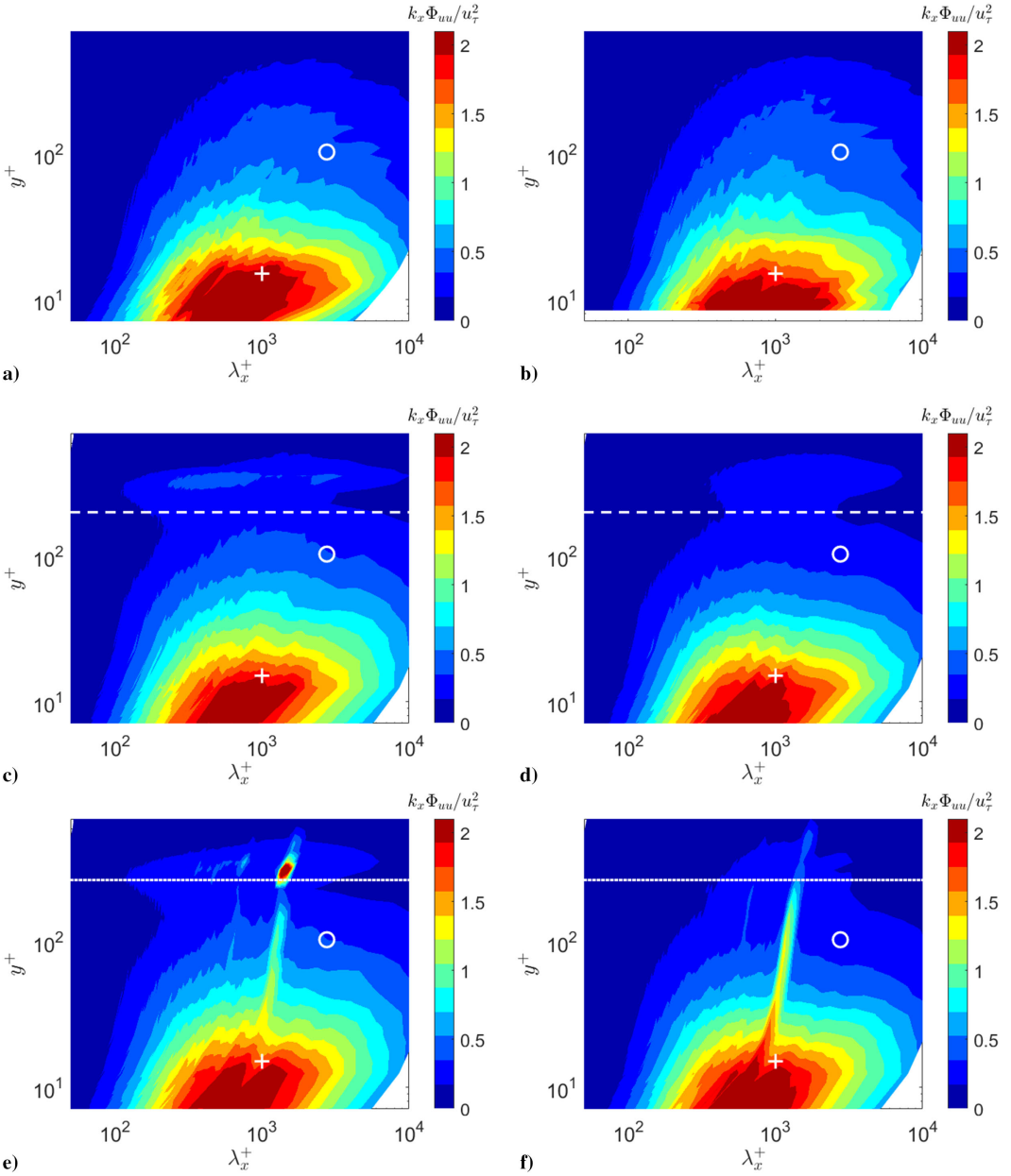

Fig. 10 Premultiplied energy spectra for a,b) canonical case; c,d) plate-only case; and e,f) plasma-on case. Measured at $x = 1.5\delta$ (a, c, e) and $x = 5\delta$ (b, d, f). Symbol "+" marks inner peak ($y^+ = 16$, $\lambda_x^+ = 1000$). Open circle marks theoretical outer peak ($y^+ = 3.9Re_\tau^{1/2}$, $\lambda_x^+ \approx 2700$). Horizontal dashed line represents actuator location, $H^+ = 200$. Horizontal dotted line represents plasma jet location, $H^+ = 265$. $f_P = 80$ Hz.

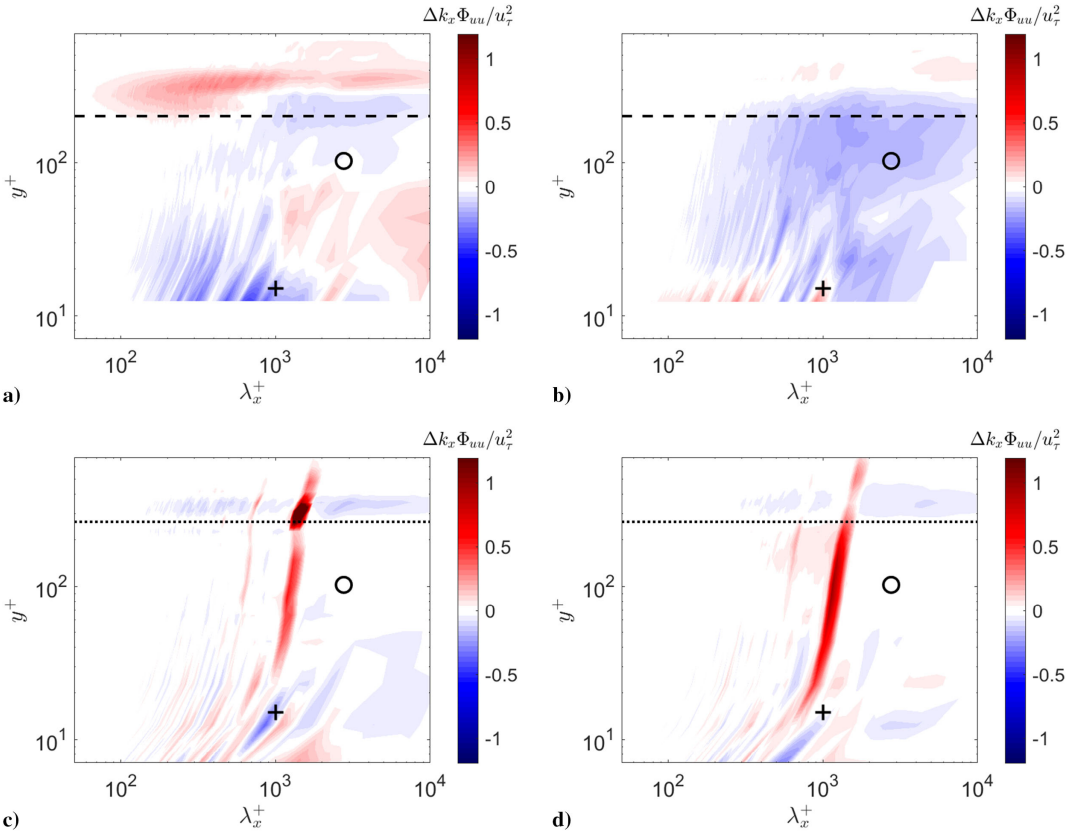

Fig. 11 Premultiplied energy spectra discrepancy for a,b) plate-only–canonical and c,d) plasma-on–plate-only. Measured at $x = 1.5\delta$ (a, c) and $x = 5\delta$ (b, d). Symbol "+" marks inner peak ($y^+ = 16$, $\lambda_x^+ = 1000$). Open circle marks theoretical outer peak ($y^+ = 3.9Re_\tau^{1/2}$, $\lambda_x^+ \approx 2700$). Horizontal dashed line represents actuator location, $H^+ = 200$. Horizontal dotted line represents plasma jet location, $H^+ = 265$. $f_P = 80$ Hz.

thickness due to the plasma jet is predictable. Near the actuator, the momentum of the plasma jet might not be well resolved by the relatively large wall-normal steps of the hot-wire measurements, leading to an overprediction of the momentum thickness, which is not seen as the jet velocity profile spreads in the wall-normal direction and is therefore better resolved, moving downstream.

The effect of plasma forcing on the relationship between turbulence intensity and local mean velocity can be seen in Fig. 9. When plasma forcing is added, there is a recovery of the linear relationship between these quantities, as seen in the canonical case, especially at the farthest downstream location. This may well demonstrate dynamic similarity to higher-Reynolds-number TBLs when the synthetic large-scale structure is present.

The premultiplied spectra of the actuated TBL are shown in Figs. 10e and 10f. The spectral signature of the synthetic LSS produced by ALSSA can be seen in the region of $y^+ = 265, \lambda_x^+ = 1600$ ($\lambda_x = 2.5\delta$). There is also a narrow band of higher than canonical energy that extends from this outer peak toward the wall, which is a manifestation of the interaction between the synthetic outer LSS and the near-wall region.

The discrepancy in premultiplied spectra between the plasma-on and plasma-off (plate-only) cases at different streamwise locations can be seen in Figs. 11c and 11d. There is a clear contribution to the energy spectra at the wavelengths associated with the plasma forcing frequency across the boundary layer. The strongest contribution is at the actuator height just downstream of the actuator, as shown in Fig. 11c, and there is an additional elongated spectral ridge that extends into the near-wall region. This signature of the LSMs induced by the actuator is similar to the signature of the boundary-layer response to dynamic roughness perturbations presented in [23], which originate within the log region closer to the wall. At the downstream location of $x = 5\delta$, shown in Fig. 11d, the peak in energy has shifted and is concentrated mostly in the log region. There are also changes in the near-wall energy peak at both downstream locations, which is an indication that the LSMs are interacting with the near-wall small-scale structures. Similar to the results in [26], the discrepancies in premultiplied spectra observed here show the receptivity of the TBL to large-scale perturbations. In this case, energy introduced through the synthetic LSMs in the outer layer is also changing the energy composition near the wall through some outer–inner interaction mechanism.

With the statistical comparison between the baseline flows established, the phase-locking method, described earlier, was implemented to analyze the effects most directly related to the disturbances introduced by the periodic plasma forcing. To begin, maps of the modal velocity and residual turbulence were computed for each streamwise measurement location. Phase maps of the modal velocity at streamwise locations of $x = 1.5\delta$ and 3δ are presented in Figs. 12a and 12b, and the results at streamwise locations of $x = 5\delta$ and 8δ are presented in Figs. 13a and 13b. There is a strong modal component of velocity at the actuator location, but there is also a significant modal velocity contribution that extends all the way toward the wall. The phase and orientation of the regions of positive modal velocity evolve with downstream distance and are consistent with the variation in convective velocity across the boundary layer. The shapes of these regions match well with both the amplitude and predicted shapes from the spatial input–output analysis of this experiment [41] and other experiments where large-scale perturbations were introduced near the wall [26]. It is of note that, in this experiment, the modal velocity pattern is well established immediately downstream of the plate, allowing for analysis of this region close to the actuator and extending downstream where the boundary layer adjusts to the synthetic LSS. The fluctuations in modal velocity around the actuator location decay slightly downstream, while the fluctuations induced in the log region appear to remain constant in amplitude.

To verify the two-dimensionality of the introduced synthetic LSS, additional experiments using two hot wires with varying spanwise separation between them were performed (see [42] for details). The same phase-locked analysis was performed for the hot wire placed at different spanwise locations, relative to the spanwise center of the

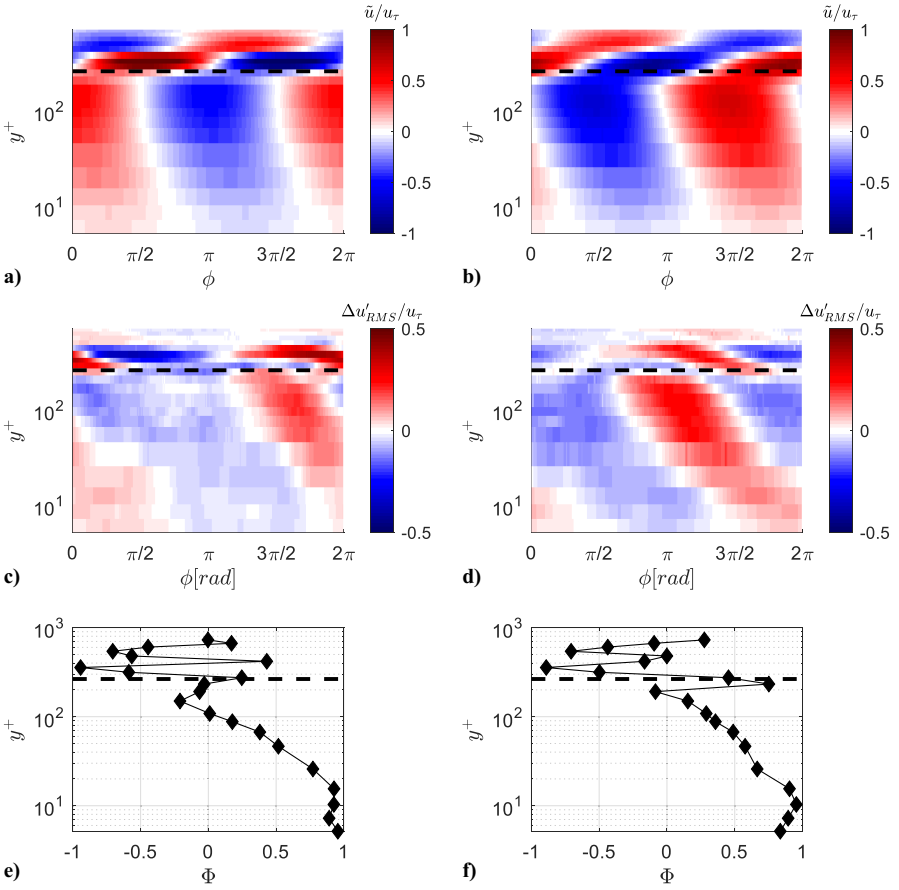

Fig. 12 Phase maps of a,b) modal velocity and c,d) residual turbulence. e,f) Profiles of modulation function Φ. Measured at $x = 1.5\delta$ (a, c, e) and $x = 3\delta$ (b, d, f). $H^+ = 200$, $f_P = 80$ Hz. Horizontal dashed line represents location of plasma forcing, $H_P^+ = 265$.

actuator plate, and the results are presented in Fig. 14. This plot demonstrates that the modal velocity is well-synchronized in the spanwise direction. This result, as well as the additional statistical analysis presented in [42] (not shown here), confirmed that the introduced synthetic LSM is essentially two-dimensional over a large spanwise extent of at least $\Delta z = \delta$.

Phase maps of the residual turbulence at each streamwise measurement location are shown in Figs. 12c, 12d, 13c, and 13d. They follow a trend similar to the modal velocity results, where there are strong fluctuations measured near the actuator location. Directly below those fluctuations, aligned in phase, there is another region of strong fluctuations in the residual turbulence. The positive fluctuations in residual turbulence above the plate are a signature of the convecting synthetic LSMs, and the fluctuations within the log or near-wall region are a signature of modulated or reorganized small-scale turbulence. This region of modulated turbulence also develops with downstream distance, locking into a preferred orientation as it approaches the farthest downstream measurement location, even as the signature of the synthetic motions above begins to diminish. The inclination of this region of modulated turbulence with respect to the wall also matches well with the observed inclination of LSS in higher-Reynolds-number boundary layers [3]. These phase maps of residual turbulence and modal velocity demonstrate the modulating effect of the synthetic LSMs and the persistence of the synthetic large-scale structure's influence on the boundary layer even at the farthest downstream measurement locations.

Profiles of the modulation coefficient Φ are shown in Figs. 12e, 12f, 13e, and 13f. At the measurement locations closest to the actuator, there is a positive peak in the modulation coefficient aligned with the location of plasma forcing. There is also a peak in the modulation coefficient in the near-wall region of the boundary layer. This near-wall peak shows that fluctuations in the modal velocity and residual turbulence are in phase and highlights the modulation effect that the synthetic LSS has, even extending into the near-wall region. Further downstream, the peak in modulation persists at the location of plasma forcing. The peak that was confined mostly to the near-wall region at earlier downstream locations has now shifted and more broadly spans the log region at farther downstream locations. This is consistent with the observations of the phase maps of modal velocity and residual turbulence, as well as the reorganization of energetic structures seen in the premultiplied energy spectra. These trends are also consistent with the interpretation that the modulation coefficient measures the phase between phase-locked motions [25].

Other modulation coefficients have been used to describe the interaction between large and small scales within canonical and actuated TBLs. The first is the so-called *R* coefficient [2], which uses a wavelength cutoff filter to separate large- and small-scale motions. The large-scale velocity signal is then correlated with the envelope of the small-scale velocity amplitude to define the modulation coefficient. This coefficient has been calculated for the actuated boundary layer with a cutoff wavelength of $\lambda_x = 1200$, and the result is presented in Fig. 15. This *R* coefficient was also shown to be closely related to skewness [24], which has also been plotted in Fig. 15. There is good agreement between the *R* coefficient and the skewness, suggesting that the cutoff wavelength used for this experiment was appropriate. Another modulation coefficient, specific to actuated TBLs, is the so-called Ψ coefficient [24]. Here the large-scale component is defined similar to the modal velocity, and the small-scale component is the triadic envelope of small-scale fluctuations, set by cutoff wavelength, which are directly coupled with the synthetic LSMs. The same wavelength cutoff was applied ($\lambda_x = 1200$) and the results are plotted along with the Φ coefficient in Fig. 15. There is good agreement between Φ and Ψ up to the actuator location around $y^+ = 200$. Once the plate wake and plasma jet are reached, there are deviations in the two modulation coefficients, which are due to the differences in the definition of the small-scale response of the TBL. The Φ modulation coefficient, which relies on phase-locked analysis and has no cutoff wavelength ambiguity, is advantageous for the current experiment

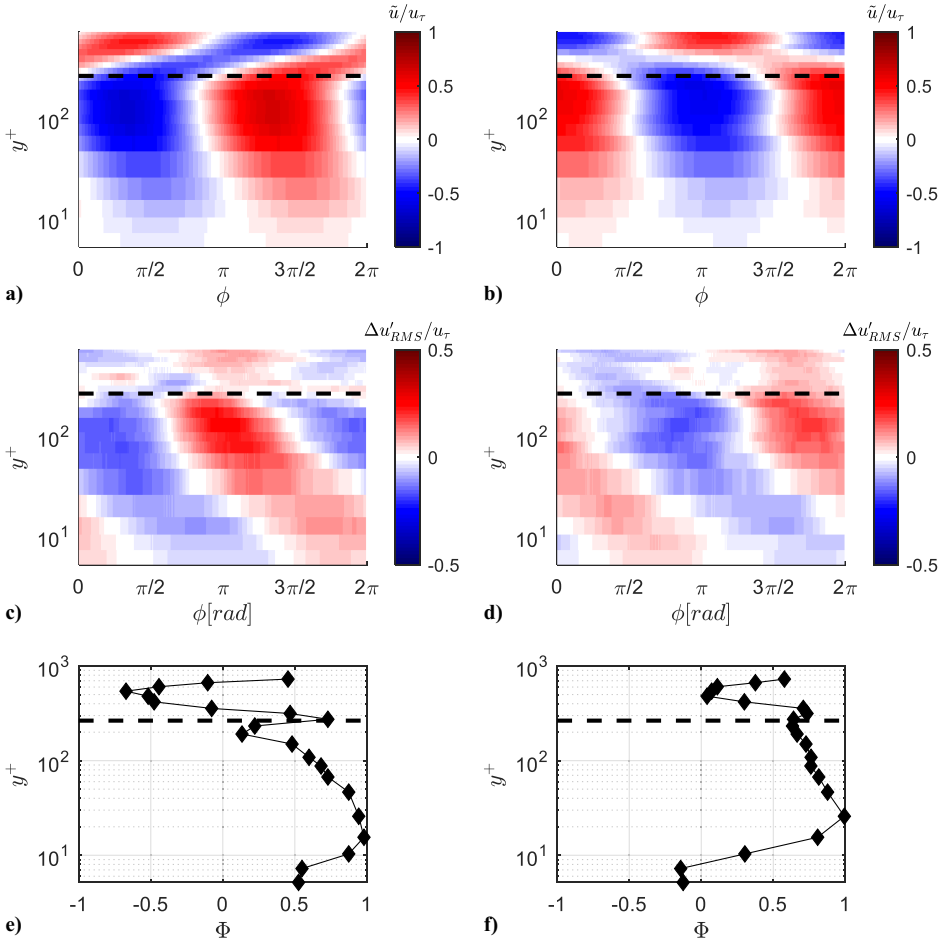

Fig. 13 Phase maps of a,b) modal velocity and c,d) residual turbulence. e,f) Profiles of modulation function Φ. Measured at $x = 5\delta$ (a, c, e) and $= 8\delta$ (b, d, f). $H^+ = 200$, $f_P = 80$ Hz. Horizontal dashed line represents location of plasma forcing, $H_P^+ = 265$.

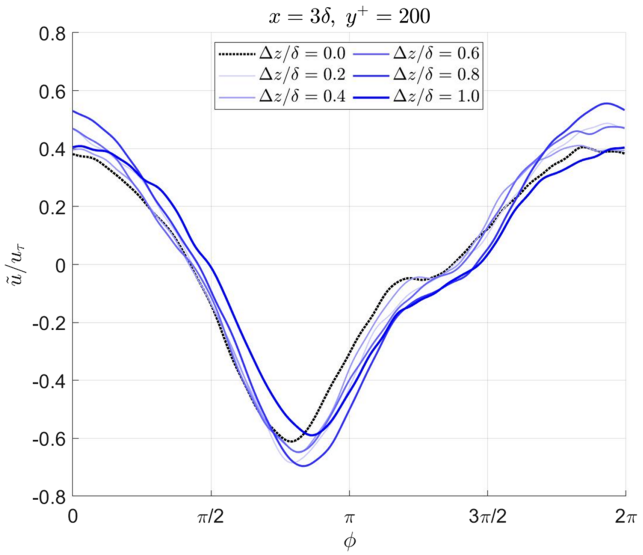

Fig. 14 Phase dependence of modal velocity at $x = 1.5\delta$ and $y^+ = 200$ for different spanwise locations, relative to the spanwise center of the actuator. $H_P^+ = 265$, $f_P = 80$ Hz.

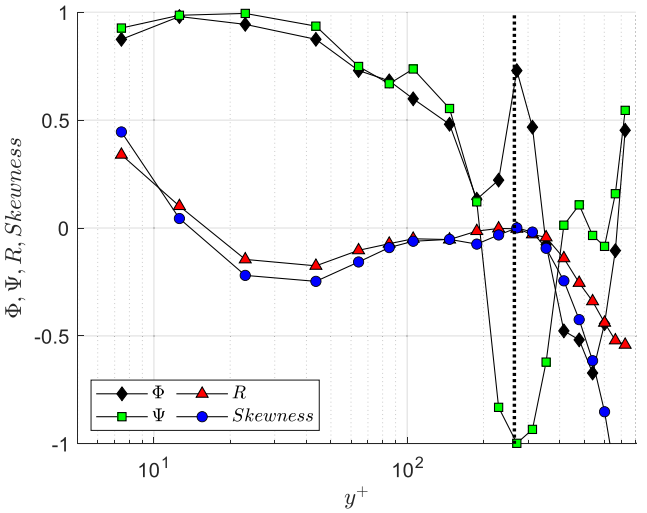

Fig. 15 Profile of modulation coefficients Φ,Ψ,R, and skewness of velocity. Location of plasma jet marked by vertical dotted line, $H_P^+ = 265$. $x = 5\delta$, $H^+ = 200$, $f_P = 80$ Hz.

where the separation of scales is so narrow. The results of Fig. 15 also demonstrate that it is as effective at measuring the interaction between scales in the TBL as the previously used modulation coefficients.

In [22,24], it was demonstrated that the Ψ coefficient experiences a sudden jump from $+1$ to -1 across the critical layer. This criterion was used in [27] to identify the location of the critical layer. For the present experiments, the Ψ coefficient is largely positive (in-phase) for both the near-wall and the log region of the TBL, as seen in Fig. 15. This suggests that the critical-layer mechanism, which plays an important role in the scale organization in the aforementioned studies, is not present in the current experiments.

The phase maps of modal velocity or residual turbulence from sequential downstream locations can also be used to determine the phase speed of large-scale disturbances, which are phase-locked with the plasma forcing. The phase speed is estimated by determining the

time delay t_n [related to phase by Eq. (2)] of certain features in the phase-locked signal, like a local minimum or a maximum, as they arrive at different downstream measurement locations. Using the relationship between phase and time from Eq. (2) and appropriately adjusting the measured time with additional actuation period delays at the farther downstream locations, the total time delay from the beginning of the actuation cycle can be found. The average phase speed between measurement locations can then be estimated using the difference in time delay and the difference in streamwise location between any two measurement locations. It is expected that the modal velocity component just above the actuator will be continuous due to the periodic and strong fluctuations induced by the plasma jet when comparing between streamwise locations. If the phase speed is correctly computed, the modal velocity at any wall-normal location can be converted from phase to pseudospace using Eq. (5), and the signal will be continuous, as demonstrated in Fig. 16b.

In Fig. 16a, the phase-dependent modal velocities from each measurement location are shown, and in Fig. 16b, the reconstructed modal velocity can be seen where the signal now appears continuous in space. This procedure can be applied across the entire boundary layer to find the phase speed of the phase-locked fluctuations. The results of this phase speed analysis are shown in Fig. 17. As shown in Fig. 17, the phase speed below the actuator location is approximately constant across all wall-normal locations. The phase speed measured using the modal velocity and residual turbulence are also equivalent within measurement error. At the closest location to the plate (see Fig. 17a), the phase speed below the actuator is approximately equal to the local mean velocity at the actuator location, $u_\varphi = 17u_\tau = 0.75U_\infty$, indicating that fluctuations in phase-locked quantities are locked with the synthetic LSS. Above the actuator height, the phase speed begins to follow the profile of the mean velocity locally. In Figs. 17b and 17c, the phase speed below the actuator is increasing but is still equal to the local mean velocity at the height of actuation. By the farthest downstream location shown in Fig. 17d, the streamwise growth in phase speed below the actuator appears to be reaching a limit around $u_\varphi = 20u_\tau = 0.89U_\infty$. The phase speed at and above the actuator

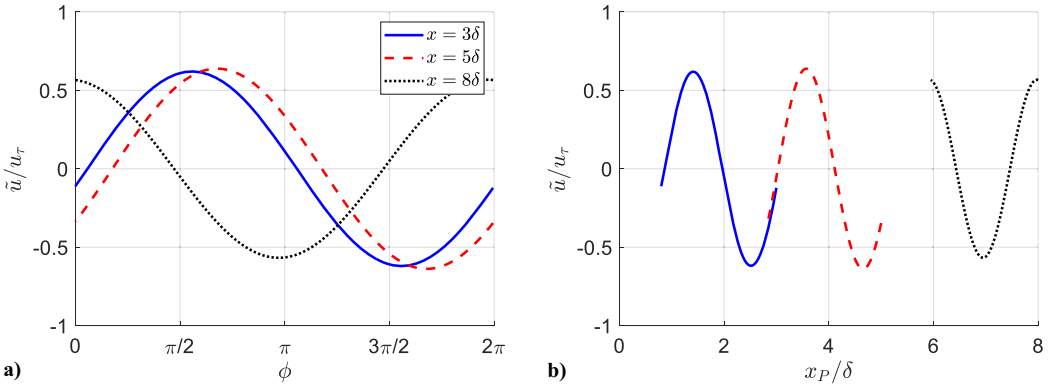

Fig. 16 Streamwise modal velocity measured at $y^+ = 200$ plotted in a) phase and b) reconstructed streamwise pseudospatial coordinate. $H^+ = 200$, $f_P = 80$ Hz.

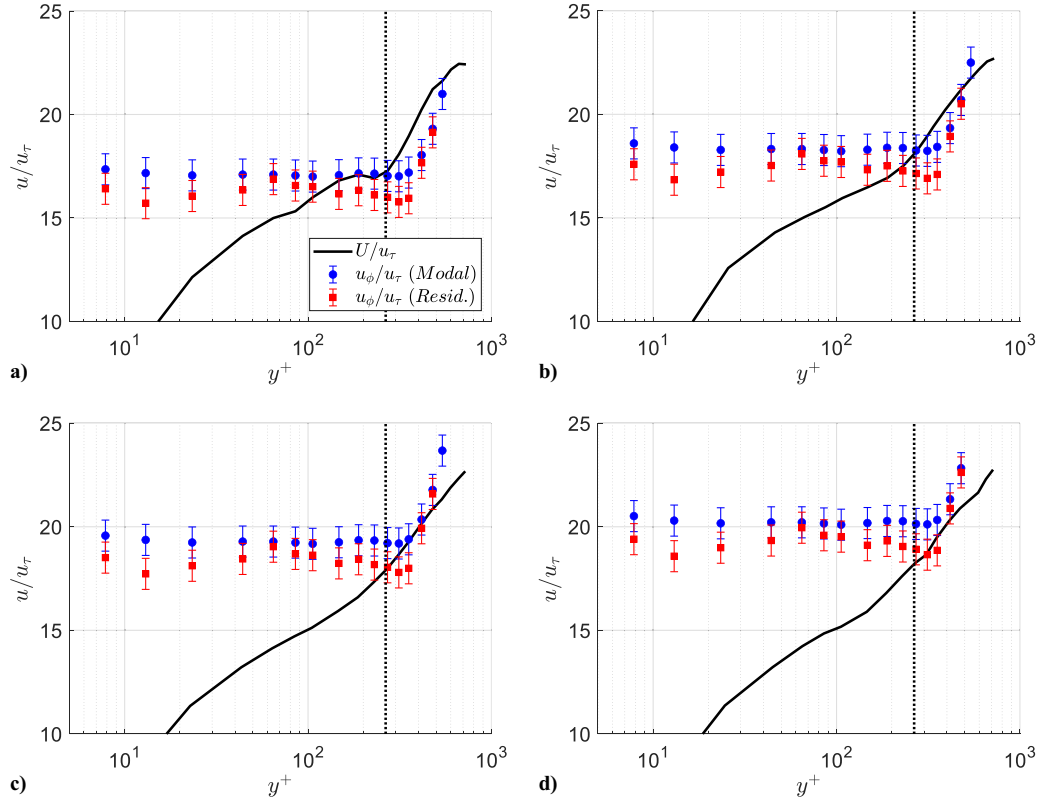

Fig. 17 Phase speed of large-scale fluctuations phase-locked with plasma forcing and mean velocity measured at a) $x = 1.5\delta$, b) $x = 3\delta$, c) $x = 5\delta$, and d) $x = 8\delta$. $H^+ = 200$, $f_P = 80$ Hz. Dotted line represents location of plasma forcing, $H_P^+ = 265$.

also begins to be consistently higher than the local mean velocity. This observation suggests that the phase speed of fluctuations below the actuator are strongly correlated with the speed of the synthetic LSSs produced by the actuator.

From Fig. 17, one can see that the criterion for the existence of the critical layer in the near-wall region is not satisfied, as all speeds in the wall-normal region, $y^+ < 200$, are lower than the convective speed of the synthetic structure. It implies, along with the earlier discussion regarding the Ψ coefficient in Fig. 15, that the turbulence modulation is not caused by the critical-layer mechanism, but rather by other mechanisms, to be discussed later in the paper.

Using the phase speed calculated above as an effective local convective velocity U_c and applying Taylor's frozen field hypothesis,

$$x_p = x_{\text{meas}} - \frac{\varphi}{2\pi}\,\frac{1}{f_p}\,U_c \tag{5}$$

the phase of each of the previous measurements was converted into a pseudospatial streamwise coordinate x_P. A pseudospatial reconstruction of the streamwise modal velocity, the wall-normal modal velocity, and the residual turbulence for the whole flowfield downstream of the actuator is presented in Fig. 18. In Figs. 18a and 18b, the reconstructions of streamwise modal velocity and residual turbulence show two distinct wall-normal regions of phase-locked fluctuation. In the streamwise modal velocity, fluctuations below the actuator appear to lead to changes above the actuator location. On the other hand, positive changes in the residual turbulence below the actuator appear to be aligned with positive changes above the actuator, but the regions are spatially distinct. The wall-normal modal velocity $\tilde{v}$ shown in Fig. 18b was computed by integrating the two-dimensional continuity equation in the wall-normal direction and imposing a no-slip condition at the wall:

$$\tilde{v}(y, x_p) = -\int_0^y \frac{\partial \tilde{u}(y, x_p)}{\partial x_p}\,\mathrm{d}y \tag{6}$$

Because the convective velocity of the streamwise modal velocity is essentially constant over the entire boundary layer, we expect that using the continuity condition to compute the wall-normal component will give a reasonable approximation. This was confirmed by the results of the spatial input output analysis, where similar shapes, phase, and amplitude were observed for the fluctuations in modal wall-normal velocity [41]. The wall-normal modal velocity does not have the same distinct wall-normal regions but instead appears in evenly spaced and periodic columns of fluctuations. This pseudospatial reconstruction gives an alternative picture of the flowfield downstream of the actuator, and the regions of modulated turbulence can be compared in space instead of phase.

Figure 19a shows the profile of the modulation coefficient Φ, at all streamwise measurement locations plotted together. Thicker and darker lines indicate a farther downstream measurement location. At the actuator location, there is a large positive correlation directly below the plate and a negative correlation above due to the plate wake. The turbulence intensity deficit below the plate and the turbulence intensity

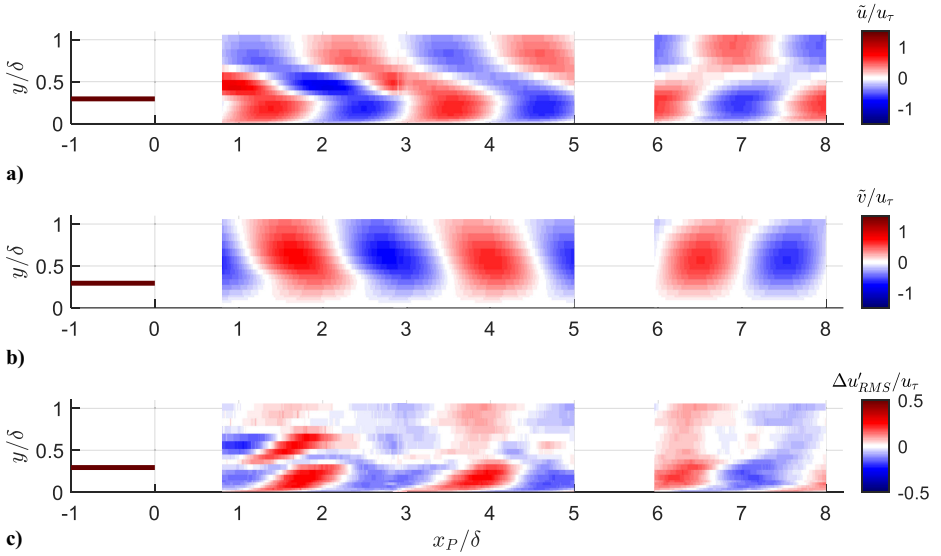

Fig. 18 Pseudospatial reconstructions of a) streamwise modal velocity, b) wall-normal modal velocity, and c) residual turbulence. $H^+ = 200$, $f_p = 80$ Hz.

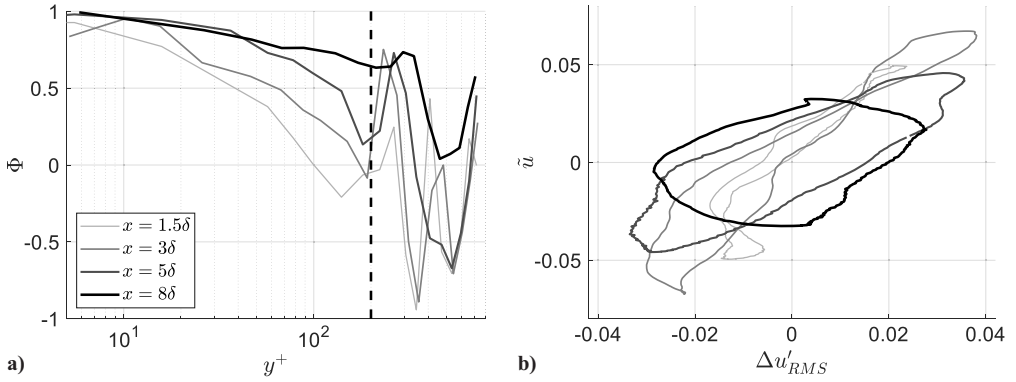

Fig. 19 a) Streamwise development of modulation coefficient Φ. Actuator location indicated by vertical dashed line. b) Relationship between fluctuations in modal velocity and residual turbulence over one actuation period measured at $y^+ = 20$. Thicker and darker lines indicate farther downstream measurement location. $H^+ = 200$, $f_P = 80$ Hz.

increase produced on top of the plate fluctuate with the plasma forcing in a wall-normal meandering motion, creating a distinct profile of Φ in that region. Of more interest is the region of strong positive modulation near the wall. This region is an indication that the near-wall turbulence is, in fact, being modulated or reorganized by synthetic LSMs. The trend moving downstream is that the positive modulation grows in magnitude (approaching unity) and in wall-normal extent. A similar trend has been documented as the Reynolds number of a canonical boundary layer is increased [2]. A quasi-steady theory, proposed in [43], hypothesizes that the flow should react to small changes in the large-scale velocity in a linear manner. Using the appropriately scaled modal velocity and residual turbulence components near the wall at each streamwise location, it was found that they are in fact linearly related in general, and the relationship becomes more linear and homogeneous with increased distance downstream. This trend can be seen in Fig. 15b, which plots the variation in modal velocity versus the residual turbulence measured at $y^+ = 20$. Consistent with the quasi-steady theory, there is a quasi-linear correlation between $\tilde{u}$ and $\Delta u'_{\text{rms}}$. It indicates that the near-wall turbulence "instantaneously" adjusts to the presence of synthetic LSS. This mostly in-phase relationship between the residual turbulence and wall-normal fluctuations in modal velocity suggests a possible mechanism in which the LSS-induced velocity transport directly modifies the velocity gradient and thus the turbulence production in the near-wall region, thereby contributing to the modulation effect.

As a final remark, the increase in correlation between scales, the changing orientation of the region of modulated turbulence, and the increasingly linear response moving downstream collectively suggest that by introducing a synthetic large-scale structure into a lower-Reynolds-number boundary layer, it gradually responds and behaves dynamically in a manner similar to a higher-Reynolds-number boundary layer.

VII. Conclusions

Experimental studies of a zero-pressure-gradient TBL response to synthetic, periodic LSSs were conducted using hot-wire anemometry. A plasma-based active flow control device was placed within the boundary layer in order to introduce periodic LSMs into the outer region. The boundary-layer Reynolds number was purposely low enough ($Re_\tau = 690$) that no naturally occurring energetic coherent LSSs were present in this region. This approach essentially uncoupled the nonlinear interaction between the large-scale structure and the near-wall turbulence present in higher-Reynolds-number boundary layers and allowed the systematic study of the effect of the large-scale structure on the near-wall turbulence. The width of the actuator was sufficient to ensure that the introduced synthetic motions are two-dimensional and that the large-scale flow structure downstream of the actuator is essentially spanwise uniform. The forcing frequency of the synthetic large-scale structure was chosen to produce the maximum modulating effect on the smaller near-wall scales. In this sense, the selected forcing frequency matched the most receptive frequencies of motion in the near-wall region, which corresponded to characteristic scales of the near-wall cycle. The actuator was also positioned such that the synthetic large-scale structure was introduced just slightly above the log region. This wall-normal location was shown to cause the largest interaction between the LSMs and small scales near the wall. A phase-locked analysis was used to quantitatively measure the modulating effect of the synthetic LSMs on the near-wall turbulence. It was demonstrated that the structures produced by the actuator modulated turbulent structures near the wall and in the log region of the boundary layer. This modulating effect persisted for several boundary-layer thicknesses downstream of the actuator, even as the organized LSMs in the outer region diminished. These regions of modulated turbulence occurred directly below peaks in residual turbulence generated by the plasma actuator as they convect downstream. The near-wall modulated regions have a very similar angular orientation to the naturally occurring structures found in higher-Reynolds-number boundary layers. Wall-normal profiles of the phase speed were also extracted from the data. The phase speed was found to be constant below the actuator and was equal to the convective speed of the synthetic structure, indicating a strong coupling between the fluctuations below the actuator and the speed of the synthetic LSSs produced by the actuator. Scale organization via the critical-layer mechanism was not observed in these studies. Instead, the results suggested that the LSS-related velocity transport toward or away from the near-wall region contributes to the modulation effect, supporting the quasi-steady theory.

Overall, the observed changes demonstrate the receptivity of the boundary layer to large-scale forcing as the boundary layer quickly adjusted to the presence of the synthetic large-scale structure. The results of this experimental investigation showed that the synthetic, periodic large-scale structure introduced by the plasma actuator had a very similar dynamic effect on the TBL as the naturally occurring LSSs in higher-Reynolds-number boundary layers. Thus, the presented approach will be useful to further study the nonlinear interaction between the outer large-scale structure and the near-wall turbulence in TBLs, as well as to explore various flow control approaches to manipulate boundary layers.

The presented work introduces a synthetic LSS into the TBL with a moderately large Reynolds number, where the naturally occurring LSS is not observed. Future studies will include similar actuation experiments on the TBL with high Reynolds numbers, where the naturally occurring LSS is present, to study modulation and reorganization effects by ALSSA on the natural large-scale structure.

Appendix:

Following a detailed accounting of experimental error, a conservative estimate of the errors (within a 95% confidence interval) associated with a comprehensive set of measured quantities of interest has been compiled in Table A1 for reference. The primary sources contributing to each experimental error have also been identified for clarity.

The wake created by the presence of the actuator plate was extracted from the modified boundary-layer profile $U_{\text{plate only}}(y)$ by subtracting the canonical boundary-layer profile $U_{\text{canonical}}(y)$ from it. Wake profiles for the first three measurement locations, normalized by the wake half-width w and velocity deficit $\Delta U_{\max}$ are presented in Fig. A1a. The streamwise development of the wake half-width and maximum velocity deficit is also presented in Fig. A1b, along with the expected streamwise growth rates for two-dimensional wakes, indicated by solid and dashed lines, respectively. The wake half-width is expected to grow at approximately $w \sim x^{0.5}$, while the maximum velocity deficit is expected to decay as $\Delta U_{\max} \sim x^{-0.5}$. These growth rates are approximations, and a virtual origin was used in order to fit the data more appropriately. Collectively, these figures demonstrate that immediately downstream of the actuator and persisting farther downstream, the wake from the actuator plate follows a canonical plane wake development [44,45].

To better understand the effect of the plasma forcing, the velocity profiles downstream of the plasma-induced jet were first measured in still air using a hot wire to determine the jet statistics. The results, normalized by the local jet half-width and the local maximum jet velocity, are shown in Fig. A2.

Table A1 Errors in measurement quantities

Quantity	Error	Error	Source
x	± 2 mm	$\pm 0.06\,\delta$	Manual positioning of traverse
y	± 0.1 mm	$\pm 2\,\nu/u_\tau$	Wall-normal positioning precision
U_∞	± 0.07 m/s	$\pm 1\%$	Manual adjustment of fan speed
δ	± 1.2 mm	$\pm 4\%$	
u	± 0.015 m/s	$\pm 0.05\,u_\tau$	Random error
$u^2_{\text{RMS}}(y^+ = 15)$	— —	-20%	Hot-wire length ($l^+ = 25$)
u_τ	± 0.03 m/s	$\pm 9\%$	Clauser method
$\tilde{u}$	± 0.006 m/s	$\pm 0.02\,u_\tau$	See Fig. 3
u'_{RMS}	± 0.006 m/s	$\pm 0.02\,u_\tau$	See Fig. 3
Φ	± 0.05	— —	
u_φ	± 0.12 m/s	$\pm 0.4\,u_\tau$	

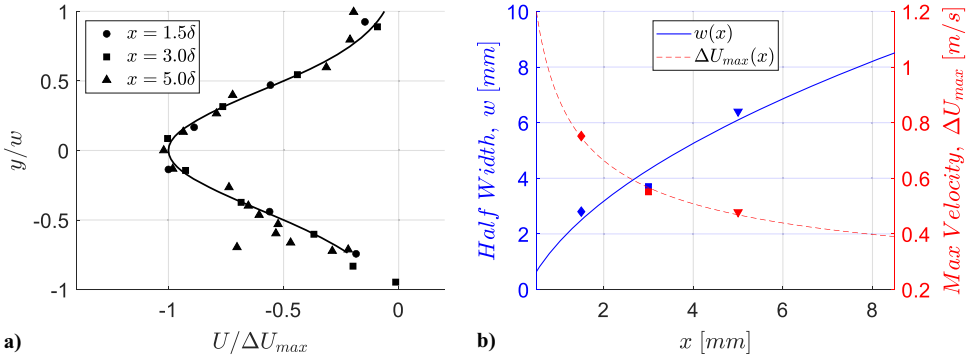

Fig. A1 a) Profiles of velocity deficit behind plate ($U_{\text{plate only}}(y) - U_{\text{canonical}}(y)$) normalized by half width and maximum velocity deficit. b) Streamwise development of half width and velocity deficit. $H^+ = 200$.

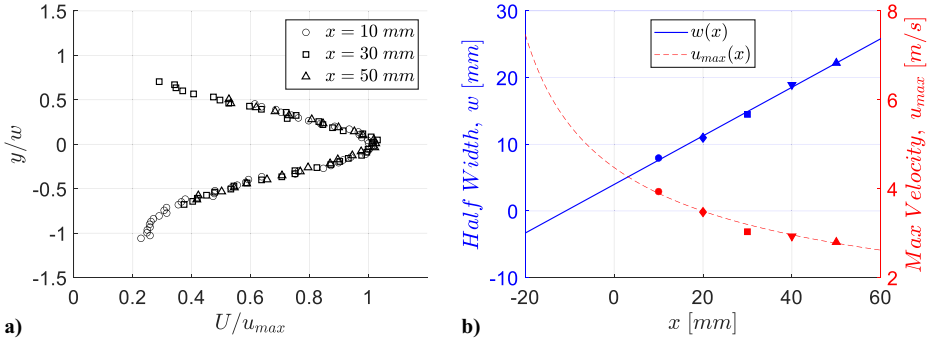

Fig. A2 a) Profiles of jet mean velocity in quiescent air normalized by half width and maximum velocity. b) Streamwise evolution of jet half width and maximum velocity. $H^+ = 200$, $f_P = 80$ Hz.

The jet velocity profile, shown in Fig. A2a, was found to have a Gaussian shape and follow a canonical growth pattern in still air, as demonstrated in Fig. A2b. The expected jet half-width growth is approximately $w \sim x$, while the jet maximum velocity is expected to decay as $u_{\max} \sim x^{-0.5}$. These growth rates are approximations, and a virtual origin was used in order to fit the data more appropriately. The maximum jet velocity was approximately 5 m/s immediately downstream of the actuator. However, it was also noted that there was a significant change in the observed jet velocity profile when it was introduced within the TBL, as shown in Fig. A3. The maximum jet mean velocity, which was extracted by subtracting the plate-only mean velocity from the plasma-on mean velocity, was 0.3 m/s or $\sim 0.04 U_\infty$, which is much less than the maximum jet velocity in still air. Thus, the accelerating effect of the plasma jet is not as pronounced when the surrounding fluid is moving in the boundary layer and the plate's wake is also interacting with the flow immediately downstream of the actuator. In spite of this, for the presented experiments, it was determined that the plasma jet was sufficiently strong, as evidenced by the ability of the plasma forcing to generate LSMs, which modulated the near-wall turbulence.

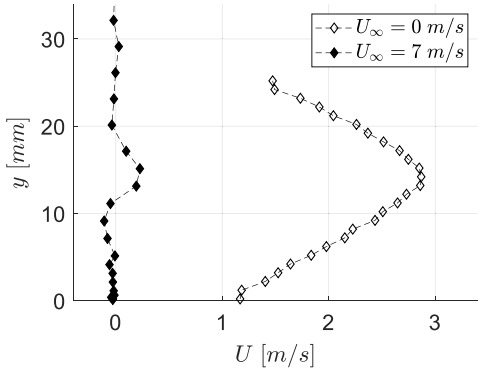

Fig. A3 Profiles of jet mean velocity in quiescent air $U_\infty = 0$ m/s and inside TBL ($U_{\text{plasma}}(y) - U_{\text{canon}}(y)$) with $U_\infty = 7$ m/s. $H^+ = 200$, $f_P = 80$ Hz.

Acknowledgment

This work is supported by the Office of Naval Research (Grant No. N00014-18-1-2534). The U.S. Government is authorized to reproduce and distribute reprints for governmental purposes notwithstanding any copyright notation thereon.

References

[1] Guala, M., Hommema, S. E., and Adrian, R. J., "Large-Scale and Very Large-Scale Motions in Turbulent Pipe Flow," *Journal of Fluid Mechanics*, Vol. 554, May 2006, pp. 521–542. https://doi.org/10.1017/S0022112006008871

[2] Mathis, R., Hutchins, N., and Marusic, I., "Large-Scale Amplitude Modulation of the Small-Scale Structures in Turbulent Boundary Layers," *Journal of Fluid Mechanics*, Vol. 628, June 2009, pp. 311–337. https://doi.org/10.1017/S0022112009006946

[3] Hutchins, N., and Marusic, I., "Large-Scale Influences in Near-Wall Turbulence," *Philosophical Transactions of the Royal Soc. A*, Vol. 365, No. 1852, 2007, pp. 647–664. https://doi.org/10.1098/rsta.2006.1942

[4] Robinson, S. K., "Coherent Motions in the Turbulent Boundary Layer," *Annual Review of Fluid Mechanics*, Vol. 23, No. 1, 1991, pp. 601–639. https://doi.org/10.1146/annurev.fl.23.010191.003125

[5] Smits, A. J., McKeon, B. J., and Marusic, I., "High-Reynolds Number Wall Turbulence," *Annual Review of Fluid Mechanics*, Vol. 43, Jan. 2011, pp. 353–375. https://doi.org/10.1146/annurev-fluid-122109-160753

[6] Hasanuzzaman, G., Merbold, S., Motuz, V., and Egbers, C., "Enhanced Outer Peaks in Turbulent Boundary Layer Using Uniform Blowing at Moderate Reynolds Number," *Journal of Turbulence*, Vol. 23, Nos. 1–2, 2022, pp. 68–95. https://doi.org/10.1080/14685248.2021.2014058

[7] Adrian, R. J., "Hairpin Vortex Organization in Wall Turbulence," *Physics of Fluids*, Vol. 19, No. 4, 2007, Paper 041301. https://doi.org/10.1063/1.2717527

[8] Kim, J., "Physics and Control of Wall Turbulence for Drag Reduction," *Philosophical Transactions of the Royal Soc. A: Mathematical, Physi-*

cal and Engineering Sciences, Vol. 369, No. 1940, 2011, pp. 1396–1411.
https://doi.org/10.1098/rsta.2010.0360

[9] Adrian, R. J., Meinhart, C. D., and Tomkins, C. D., "Vortex Organization in the Outer Region of the Turbulent Boundary Layer," *Journal of Fluid Mechanics*, Vol. 422, Nov. 2000, pp. 1–54.
https://doi.org/10.1017/S0022112000001580

[10] de Silva, C. M., Hutchins, N., and Marusic, I., "Uniform Momentum Zones in Turbulent Boundary Layers," *Journal of Fluid Mechanics*, Vol. 786, Jan. 2016, pp. 309–331.
https://doi.org/10.1017/jfm.2015.672

[11] Head, M. R., and Bandyopadhyay, P., "New Aspects of Turbulent Boundary-Layer Structure," *Journal of Fluid Mechanics*, Vol. 107, June 1981, pp. 297–338.
https://doi.org/10.1017/S0022112081001791

[12] Mathis, R., Hutchins, N., and Marusic, I., "A Predictive Inner-Outer Model for Streamwise Turbulence Statistics in Wall-Bounded Flows," *Journal of Fluid Mechanics*, Vol. 681, Aug. 2011, pp. 537–566.
https://doi.org/10.1017/jfm.2011.216

[13] Andreolli, A., Gatti, D., Vinuesa, R., Örlü, R., and Schlatter, P., "Separating Large-Scale Superposition and Modulation in Turbulent Channels," *Journal of Fluid Mechanics*, Vol. 958, March 2023, Paper A37.
https://doi.org/10.1017/jfm.2023.103

[14] Marusic, I., and Monty, J. P., "Attached Eddy Model of Wall Turbulence," *Annual Review of Fluid Mechanics*, Vol. 51, Jan. 2019, pp. 49–74.
https://doi.org/10.1146/annurev-fluid-010518-040427

[15] Schatzman, D. M., and Thomas, F. O., "An Experimental Investigation of an Unstready Adverse Pressure Gradient Turbulent Boundary Layer: Embedded Shear Layer Scaling," *Journal of Fluid Mechanics*, Vol. 815, March 2017, pp. 592–642.
https://doi.org/10.1017/jfm.2017.65

[16] Coles, D. E., and Hirst, E. A., "Computation of Turbulent Boundary Layers: Compiled Data," *AFOSR-IFP*, Vol. 2, Stanford Univ., 1968.

[17] Alfredsson, P. H., and Örlü, R., "Large-Eddy BreakUp Devices—A 40 Years Perspective from a Stockholm Horizon," *Flow Turbulence and Combust*, Vol. 100, No. 4, 2018, pp. 877–888.
https://doi.org/10.1007/s10494-018-9908-4

[18] Corke, T. C., Guezennec, Y., and Nagib, H. M., "Modification in Drag of Turbulent Boundary Layers Resulting from Manipulation of Large-Scale Strucutres," NASA- CR-3444, 1981.

[19] Savill, A. M., and Mumford, J. C., "Manipulations of Turbulent Boundary Layers by Outer-Layer Devices: Skin-Friction and Flow-Visualization Results," *Journal of Fluid Mechanics*, Vol. 191, June 1988, pp. 389–418.
https://doi.org/10.1017/S0022112088001624

[20] Smith, A. E., and Gordeyev, S., "Aero-Optical Mitigation of Turbulent Boundary Layers Using Large-Eddy Break-Up Devices," *52nd Aerospace Sciences Meeting*, AIAA Paper 2014-0321, 2014.
https://doi.org/10.2514/6.2014-0321

[21] Marusic, I., Chandran, D., Rouhi, A., Fu, M. K., Wine, D., Holloway, B., Chung, D., and Smits, A. J., "An Energy-Efficient Pathway to Turbulent Drag Reduction," *Nature Communications*, Vol. 12, No. 1, 2021, Paper 5805.
https://doi.org/10.1038/s41467-021-26128-8

[22] McKeon, B. J., Jacobi, I., and Duvvuri, S., "Dynamic Roughness for Manipulation and Control of Turbulent Boundary Layers: An Overview," *AIAA Journal*, Vol. 56, No. 6, 2018, pp. 2178–2193.
https://doi.org/10.2514/1.J056764

[23] Jacobi, I., and McKeon, B. J., "Dynamic Roughness Perturbation of a Turbulent Boundary Layer," *Journal of Fluid Mechanics*, Vol. 688, Dec. 2011, pp. 258–296.
https://doi.org/10.1017/jfm.2011.375

[24] Duvvuri, S., and McKeon, B. J., "Triadic Scale Interactions in a Turbulent Boundary Layer," *Journal of Fluid Mechanics*, Vol. 767, March 2015, Paper R4.
https://doi.org/10.1017/jfm.2015.79

[25] Duvvuri, S., and McKeon, B., "Phase Relations in a Forced Turbulent Boundary Layer: Implications for Modelling of High Reynolds Number Wall Turbulence," *Philosophical Transactions of the Royal Soc. A*, Vol. 375, No. 2089, 2017, Paper 20160080.
https://doi.org/10.1098/rsta.2016.0080

[26] Huynh, D., and McKeon, B., "Characterization of the Spatio-Temporal Repsonse of a Turbulent Boundary Layer to Dynamic Roughness," *Flow Turbulence and Combustion*, Vol. 104, Nos. 2–3, 2020, pp. 293–316.
https://doi.org/10.1007/s10494-019-00069-1

[27] Ranade, P., Duvvuri, S., McKeon, B., Gordeyev, S., Christensen, K., and Jumper, E. J., "Turbulence Amplitude Amplification in an Externally Forced, Subsonic Turbulent Boundary Layer," *AIAA Journal*, Vol. 57, No. 9, 2019, pp. 3838–3850.
https://doi.org/10.2514/1.J057871

[28] Patel, M. H., "On Turbulent Boundary Layers in Oscillatory Flow," *Proceedings of the Royal Soc. of London. A. Mathematical and Physical Sciences*, Vol. 353, No. 1672, 1977, pp. 121–144.
https://doi.org/10.1098/rspa.1977.0025

[29] Corke, T. C., and Thomas, F. O., "Active and Passive Turbulent Boundary-Layer Drag Reduction," *AIAA Journal*, Vol. 56, No. 10, 2018, pp. 3835–3847.
https://doi.org/10.2514/1.J056949

[30] Duong, A. H., Corke, T. C., and Thomas, F. O., "Characteristics of Drag-Reduced Turbulent Boundary Layers with Pulsed-Direct-Current Plasma Actuation," *Journal of Fluid Mechanics*, Vol. 915, May 2021, Paper A113.
https://doi.org/10.1017/jfm.2021.167

[31] Thomas, F. O., Corke, T. C., Duong, A., Midya, S., and Yates, K., "Turbulent Drag Reduction Using Pulsed-DC Plasma Actuation," *Journal of Physics D: Applied Physics*, Vol. 52, No. 43, 2019, Paper 434001.
https://doi.org/10.1088/1361-6463/ab3388

[32] Thomas, F. O., Corke, T. C., and Duong, A. H., "Airfoil Friction Drag Reduction with Net Power Savings Using Pulsed-Direct-Current Plasma Actuation," *AIAA Journal*, Vol. 61, No. 9, 2023, pp. 4045–4055.
https://doi.org/10.2514/1.J062627

[33] Hutchins, N., Nickels, T. B., Marusic, I., and Chong, M. S., "Hot-Wire Spatial Resolution Issues in Wall-Bounded Turbulence," *Journal of Fluid Mechanics*, Vol. 635, Sept. 2009, pp. 103–136.
https://doi.org/10.1017/s0022112009007721

[34] Thomas, F. O., Corke, T. C., Iqbal, M., Kozlov, A., and Schatzman, D., "Optimization of Dielectric Barrier Discharge Plasma Actuators for Active Aerodynamic Flow Control," *AIAA Journal*, Vol. 47, No. 9, 2009, pp. 2169–2178.
https://doi.org/10.2514/1.41588

[35] Wicks, M., and Thomas, F. O., "Effect of Relative Humidity on Dielectic Barrier Discharge Plasma Actuator Body Force," *AIAA Journal*, Vol. 53, No. 9, 2015 pp. 2801–2805.
https://doi.org/10.2514/1.J053810

[36] Lozier, M., Midya, S., Thomas, F. O., and Gordeyev, S., "Experimental Studies of Boundary Layer Dynamics Using Active Flow Control of Large-Scale Structures," TSFP-11, 2019, Paper 5B-3.

[37] Jiménez, J., Hoyas, S., Simens, M. P., and Mizuno, Y., "Turbulent Boundary Layers and Channels at Moderate Reynolds Number," *Journal of Fluid Mechanics*, Vol. 657, Aug. 2010, pp. 335–360.
https://doi.org/10.1017/s0022112010001370

[38] Lozier, M. E., Thomas, F. O., and Gordeyev, S., "Streamwise Evolution of Turbulent Boundary Layer Response to Active Control Actuator," *AIAA Scitech 2020 Forum*, AIAA Paper 2020-0097, 2020.
https://doi.org/10.2514/6.2020-0097

[39] Luchik, T. S., and Tiederman, W. G., "Timescale and Structure of Ejections and Busts in Turbulent Channel Flows," *Journal of Fluid Mechanics*, Vol. 174, Jan. 1987, pp. 529–552.
https://doi.org/10.1017/S0022112087000235

[40] Hasanuzzaman, G., Merbold, S., Cuvier, C., Motuz, V., Foucaut, J. M., and Egbers, C., "Experimental Investigation of Tubeulent Boundary Layers at High Reynolds Number with Uniform Blowing, Part I: Statistics," *Journal of Turbulence*, Vol. 21, No. 3, 2020, pp. 129–165.
https://doi.org/10.1080/14685248.2020.1740239

[41] Liu, C., Gluzman, I., Lozier, M., Midya, S., Gordeyev, S., Thomas, F. O., and Gayme, D. F., "Spatial Input–Output Analysis of Large-Scale Structures in Actuated Turbulent Boundary Layers," *AIAA Journal*, Vol. 60, No. 11, 2022, pp. 6313–6327.
https://doi.org/10.2514/1.J061706

[42] Lozier, M., "Characterization of Turbulent Boundary Layer Dynamics via Active Manipulation of Large-Scale Structures," 2023.
https://doi.org/10.7274/70795715s1m

[43] Zhang, C., and Chernyshenko, S. I., "Quasisteady Quasihomogeneous Description of the Scale Interactions in Near-Wall Turbulence," *Physical Review Fluids*, Vol. 1, No. 1, 2016, Paper 014401.
https://doi.org/10.1103/PhysRevFluids.1.014401

[44] Schlicting, H., *Boundary Layer Theory*, 9th ed., Springer, Berlin, 2017, pp. 653–680.
https://doi.org/10.1007/978-3-662-52919-5

[45] Liu, X., Thomas, F. O., and Nelson, R. C., "An Experimental Investigation of the Planar Turbulent Wake in Constant Pressure," *Physics of Fluids*, Vol. 14, No. 8, 2002, pp. 2817–2838.
https://doi.org/10.1063/1.1490349

L. Ukeiley
Associate Editor